VLASOV THEORY OF THE EQUILIBRIUM STRUCTURE OF TANGENTIAL DISCONTINUITIES IN SPACE PLASMAS

M. ROTH and J. DE KEYSER
Belgian Institute for Space Aeronomy, B-1180 Brussels, Belgium

and

M.M. KUZNETSOVA
Laboratory for Extraterrestrial Physics,
NASA Goddard Space Flight Center, Greenbelt, Maryland, U.S.A., and
IKI, Space Research Institute, Moscow, Russia

(Received 5 December, 1995)

Abstract. Extensive theoretical work has been performed on the equilibrium structure of tangential discontinuities (TDs) in collisionless plasmas. This paper reviews kinetic models based on steady-state solutions of the Vlasov equation. It is shown that most of the existing models are special cases of a generalized multi-species model. In this generalized model all particle populations – from both outer regions and from inside the layer – are described using a unique formalism for the velocity distribution functions. Because of their historical importance, the Harris and Sestero models are reviewed and deduced from the generalized model. The Lee and Kan model is also a special case of the generalized model. The generalized model, however, is also able to describe TDs with velocity shear and large angles of magnetic field rotation. Such a multi-species model with a large number of free parameters and different gradient scales illustrates many observable features of TDs, including their multiscale fine structure. Particular attention is paid to the magnetopause. Observed magnetopause crossings are simulated. The effects of the relative flow velocity and asymmetrical magnetic field profiles on the structure of the magnetopause and on its stability with respect to tearing perturbations are discussed. We also present calculations that demonstrate the potential of the generalized model in explaining the origin of discrete auroral arcs. Numerical simulations of solar wind TDs with heavy ions and a large spectrum of thicknesses are also feasible. This indicates that such a model is of fundamental importance for understanding the detailed structure of solar wind TDs, like those observed by the interplanetary spacecraft ULYSSES. The problems associated with the one-dimensional, time-independent Vlasov approach are discussed and a variational principle is suggested to reduce the arbitrariness resulting from the large number of free parameters.

Table of Contents

Space Science Reviews **76:** 251–317, 1996.

1. Introduction

Space plasmas have a natural tendency to fill up distinct regions, separated by a number of boundary surfaces (Fälthammar *et al.*, 1978). These boundary layers separate plasmas possessing different parameters and constitute electric current sheets. Space exploration has amply demonstrated the existence of such layers, e.g., the magnetopause (the outer boundary of the Earth's magnetosphere) and the plasma sheet in the magnetospheric tail. Similar boundary layers resulting from the interaction of the solar wind with the magnetic fields of Mercury, Jupiter, Saturn, Uranus and Neptune have also been observed. The overall structure of the heliosphere (the realm dominated by the solar wind) is largely determined by the presence of the heliospheric current sheet. On the interstellar and intergalactic scales, space in general is expected to have a 'cellular' structure (Alfvén, 1981).

Current layers in space may be very thin, sometimes only a few ion Larmor radii (gyroradii). The kinetic theory is therefore the most appropriate tool to study the equilibrium structure and stability properties of these plasma regions. A kinetic investigation of plasma processes within such layers is very important, as these processes control the mass and energy exchanges between adjacent regions. As a typical example, the overall dynamics of the Earth's magnetosphere is controlled by kinetic processes in magnetospheric boundary layers; as such, these processes govern important phenomena like magnetospheric substorms and aurorae.

Different types of boundary layers may form in space plasmas (see, for instance, the paper by Hudson (1970) where different types of discontinuity are discussed). A first type may be classified as 'tangential discontinuity' (TD). This type of discontinuity describes a structure where the magnetic field and the flow are tangential to the boundary surface. 'Contact discontinuities' likewise exhibit no mass transport through the surface, but do have a nonzero normal magnetic field component.

'Perpendicular shocks' and 'inclined shocks' are structures where there is mass transport across the discontinuity. Inclined shocks with small normal magnetic field (B_n) and normal plasma velocity (V_n) have been described by Lembege and Pellat (1982) as slightly perturbed TDs, in an attempt to model the magnetotail plasma sheet where $V_n = 0$ and $B_n \neq 0$. They extend the well-known symmetrical Harris equilibrium model (Harris, 1962); a generalization of their approach to the case of asymmetrical TDs, however, is needed to describe more complex inclined shock structures.

In this review we will only consider tangential discontinuities. This type of discontinuity is of importance in many different areas of solar-terrestrial physics.

There is some observational evidence for TDs at the magnetopause. The most pertinent of these observations come from magnetopause crossings in the International Sun Earth Explorer (ISEE) and Active Magnetospheric Particle Tracer Experiment (AMPTE) data that do not show an associated adjacent magnetospheric boundary layer (Cargill and Eastman, 1991, and references therein). Typical magnetopause current layer widths are 400–1000 km, corresponding to just a few ion Larmor radii (Berchem and Russell, 1982a).

Some magnetospheric boundary layers can also be identified as TDs. This is the case for the magnetotail current layer, the plasmasheet boundary layer (PSBL) in the tail, or the boundaries of some plasmasheet clouds immersed in the central plasma sheet. The electric structure of some of these boundary layers is related to the formation of discrete auroral arcs (Roth *et al.*, 1993). The plasmapause too has been treated as a TD (Roth, 1976).

TDs are also a prevalent feature of the solar wind. Discontinuities in the interplanetary magnetic field from Explorer 43 data were identified by Burlaga *et al.* (1977) under a variety of interplanetary conditions. Both tangential discontinuities (TDs) and rotational discontinuities (RDs) were identified, the ratio of TDs to RDs being 2.8 to 1. Even in regions where Alfvénic fluctuations are most pronounced, the ratio of TDs to RDs was found to be approximately one. First results from ULYSSES magnetic field and plasma data indicate that TDs are a common feature also at high heliographic latitudes (Tsurutani *et al.*, 1994). Solar wind TDs are often much wider than the magnetopause current layer: widths corresponding to 1.5–80 Larmor radii (150–8000 km) have been observed (Burlaga *et al.*, 1977). In addition, the large density and temperature gradients typical for some magnetospheric TDs are not often found in the solar wind. Observations of the fine-scale characteristics of interplanetary sector boundaries by HELIOS 1 have shown that a large number of these boundaries should be considered TDs rather than RDs, with a large angle of magnetic field rotation (120° to 180°) and usually accompanied by a large dip in magnetic field strength (Behannon *et al.*, 1981).

Current and future missions, like INTERBALL, CLUSTER, WIND and GEOTAIL, have the potential to revolutionize our understanding of TDs. In view of the high quality and improved time resolution of the data obtained onboard these spacecraft, there is a renewed interest in the development of kinetic models for the interpretation of thin plasma boundaries.

This paper will review the kinetic theory of TDs. It should be noted that Vlasov theories of plane TDs yield non-unique solutions. In a macroscopic description, any pressure profile $P(x)$ and magnetic field $B(x)$ related by $P + B^2/8\pi = \text{constant}$ define an equilibrium solution. In a Vlasov description, this non-uniqueness shows up in the arbitrariness with which particle velocity distribution functions can be chosen. Only consideration of particle accessibility (i.e., tracing the origin of the populations) can remove this non-uniqueness (Whipple *et al.*, 1984). In this review, we will not address this accessibility question, nor the temporal behavior of TDs; we will only consider steady-state plane TDs and limit our choice to single-valued distribution functions of the constants of motion of the particles.

Vlasov equilibrium models of tangential discontinuities in collisionless plasmas have been described by, e.g., Grad (1961), Harris (1962), Nicholson (1963), Sestero (1964, 1966), Alpers (1969), Kan (1972), Roth (1976, 1978, 1979, 1980, 1983, 1986), Lemaire and Burlaga (1976), Channell (1976), Lee and Kan (1979), Roth *et al.* (1990, 1993), Kuznetsova *et al.* (1994), Kuznetsova and Roth (1995). Table I summarizes the characteristics of most of these one-dimensional models.

In the general case, the number of ion and electron populations can be arbitrarily large. The particle populations can be subdivided into three groups: the two 'outer' sides of the transition and its 'inner' region. For instance, for magnetopause modeling it is reasonable to introduce magnetosheath, magnetospheric, and trapped populations. The density of magnetosheath particles tends to zero on the magnetospheric side ($x \to +\infty$), while the density of magnetospheric particles tends to zero on the magnetosheath side ($x \to -\infty$). The inner populations are confined inside the magnetopause, their density having a maximum inside the current layer and tending to zero on both sides ($x \to \pm\infty$). The inner populations are especially important in TDs with large magnetic shear. In most models, inner populations are described by the well known analytical Harris model (Harris, 1962). Other forms of inner distributions have also been introduced, e.g., in the paper of Nicholson (1963). The distribution functions of the outer populations explicitly contain some arbitrary cutoff factors in phase space to describe the fact that charged particles from one side cannot penetrate arbitrarily deep into the other side, thereby circumventing the accessibility problem. These cutoff factors are usually chosen in the form of step functions (e.g., Sestero, 1964, 1966; Lemaire and Burlaga, 1976; Roth, 1976, 1978, 1979, 1980) or error functions (e.g., Alpers, 1969; Lee and Kan, 1979; Roth *et al.*, this review) because they lead to analytical expressions for the moments of the distribution functions. The choice of error functions allows one to introduce arbitrary gradient scales $l^{\nu}_{y,z}\rho^{\nu} \geq \rho^{\nu}$ (ρ^{ν} is the gyroradius of the ν'th species). Even for step-like cutoffs the characteristic thickness of the TD can not be less than one electron gyroradius ρ^- (in electron-dominated layers, where ions are isotropic, and the electric current is only carried by electrons), or one ion gyroradius ρ^+ (in ion-dominated layers, where the electric current is carried by ions).

TABLE I
Characteristics of kinetic TD models

Models	Properties
Grad (1961): A *unique* and monotone **B**-field profile exists for the *thinnest* transition describing the exponential decrease of a field-free plasma into a unidirectional magnetic field region, if there are no 'inner' particles and if the asymptotic distributions are isotropic	**Electrostatics** Charge separation effects in the case of particles of different masses are ignored. **Thickness** $c/\omega_p = \rho$
Harris (1962): Plasma slab separating plasma-free regions of oppositely directed magnetic fields ($\mp\mathbf{B}_R$ along the z axis). The inner populations of electrons ($-$) and protons ($+$) are described by Maxwellian distribution functions shifted along the v_y axis by the drift velocity $\mathcal{U}_H^{\mp} = \pm 2c\mathcal{T}/eB_R\mathcal{L}_H$ ($\mathcal{L}_H$=characteristic thickness).	**Electrostatics** Electric field vanishes in the reference system where $\mathcal{U}_H^- = -\mathcal{U}_H^+$. **Thickness** $\mathcal{L}_H > \mathcal{L}_D$
Nicholson (1963): Plasma slab separating plasma-free regions of constant magnetic field, the field being in the same direction on the two sides of the slab. The inner populations of electrons and protons have velocity distribution functions that differ from Maxwellians to the extent that a parameter a entering into the characteristic length differs from zero.	**Electrostatics** Exact charge neutrality. This condition fixes the parameter a and the thickness. **Thickness** ρ^+
Sestero (1964): Magnetized plasma on both sides without inner populations. Unidirectional magnetic field. No change in the plasma velocity across the plasma sheet. Two plasma components (electrons and ions). Asymptotic isothermal plasma ($\mathcal{T} = T^+(\pm\infty) = T^-(\pm\infty)$).	**Electrostatics** Charge neutral approximation. Non-zero normal electric field. **Thickness** ρ^- or ρ^+
Sestero (1966): Magnetized plasma on both sides without inner populations. Unidirectional magnetic field. Change in the plasma bulk velocity in the direction perpendicular to the field. Two plasma components (electrons and ions). Asymptotic isothermal plasma ($\mathcal{T} = T^+(\pm\infty) = T^-(\pm\infty)$). The maximum velocity shear is the thermal velocity of the particles carrying the current (ions in ion-dominated layers, electrons in electron-dominated layers).	**Electrostatics** Charge neutral approximation. Non-zero normal electric field. **Thickness** ρ^- or ρ^+

TABLE I

Characteristics of kinetic TD models (continued)

Models	Properties
Alpers (1969): A whole class of distribution functions are constructed by prescribing the magnetic field profile and a bulk velocity profile in the direction of the magnetic field. Magnetic shear is included ($B_y \neq 0$). Two plasma components (electrons and ions). Asymptotic isothermal plasma ($\mathcal{T} = T^+(\pm\infty) = T^-(\pm\infty)$). No inner populations.	**Electrostatics** Exact charge neutrality. **Thickness** $\geq \rho^+$
Roth (1976): Magnetized plasma on both sides without inner populations. Unidirectional magnetic field. Change in the plasma bulk velocity in the direction perpendicular to the field. Multi-species plasma with different densities and temperatures.	**Electrostatics** Charge neutral approximation. Non-zero normal electric field. **Thickness** ρ^- or ρ^+
Lemaire and Burlaga (1976): Magnetized plasma on both sides without inner populations. Magnetic shear is included ($B_y \neq 0$). No change in the plasma velocity across the plasma sheet. Multi-species plasma with different densities and temperatures.	**Electrostatics** Charge neutral approximation. Non-zero normal electric field. **Thickness** ρ^- or ρ^+
Roth (1978, 1979, 1980): Magnetized plasma on both sides with or without inner populations. Magnetic shear ($B_y \neq 0$). Shear in the plasma bulk velocity ($V_y \neq 0$, $V_z \neq 0$). One single formalism for inner and outer populations. Multi-species plasma with different densities and temperatures. Asymptotic temperature anisotropies ($\mathcal{T}_\perp \neq \mathcal{T}_\parallel$).	**Electrostatics** Charge neutral approximation. Non-zero or zero normal electric field. **Thickness** $> \mathcal{L}_D$ (inner only), ρ^- or ρ^+
Lee and Kan (1979): Magnetized plasma on both sides with or without inner populations. Magnetic shear ($B_y \neq 0$). Shear in the plasma bulk velocity ($V_y \neq 0$, $V_z \neq 0$). Different formalisms for inner and outer populations. Two plasma components (protons, electrons) with different densities and temperatures.	**Electrostatics** Charge neutral approximation or exact charge neutrality. **Thickness** $\geq \rho^+$
This review: The step functions describing the cutoff factors in the previous model of Roth (1978, 1979, 1980) are replaced by error functions. Other characteristics of this generalized model are unchanged, except that temperature anisotropies are not considered in the velocity distribution functions.	**Electrostatics** Charge neutral approximation. Non-zero or zero normal electric field. **Thickness** $> \mathcal{L}_D$ (inner only); $\geq \rho^-$

However, in symmetrical transitions of the Harris type, the minimum thickness can approach the Debye length $\mathcal{L}_D$. In the general case the characteristic thickness of the transition is determined by the gradient scales of all populations collectively. Thin electron layers appear to be extremely unstable (Roth *et al.*, 1993; Drake *et al.*, 1994), so it is usual to consider only layers with a characteristic thickness of a few ion gyroradii.

In summary, the existing one-dimensional Vlasov models can be characterized by the following set of attributes:

– The number of different particle populations (outer, and inner). For instance, the models by Harris (1962) and Nicholson (1963) include only inner populations of electrons and protons, while Sestero (1964, 1966) and Alpers (1969) introduced only outer particles. Both inner and outer populations were incorporated by Roth (1978, 1979, 1980) and Lee and Kan (1979). Multi-species plasma with different densities, ion charges and temperatures were considered by Lemaire and Burlaga (1976) and Roth (1976, 1978, 1979, 1980) (including asymptotic temperature anisotropies).

– Assumptions about the charge neutrality.

– The form of the cutoff functions and corresponding gradient scales that control the thickness of the TD.

– The degree of asymmetry in boundary conditions that can be described by the model (e.g., the velocity shear, the angle of magnetic field rotation θ, density and temperature asymmetries). For instance, models by Sestero (1966) and Roth (1976), where velocity shear was taken into account, imply unidirectional magnetic fields ($\theta = 0$). The model by Alpers (1969), which has no inner populations, can describe TDs with velocity shear but small magnetic shear ($\theta < 90^\circ$). The unified model by Lee and Kan (1979) can describe asymmetric TDs with zero velocity shear and arbitrary magnetic shear (including $\theta > 90^\circ$) as well as TDs with finite velocity shear and small magnetic shear ($\theta < 90^\circ$), but due to different formalisms for inner and outer populations their model is unable to describe TDs with both velocity shear and large magnetic shear ($\theta > 90^\circ$).

A generalized multi-species Vlasov model of TDs is presented in this review. In this model all particle populations (from both outer regions and from inside the layer) are described using a unique formalism for the velocity distribution functions. Most of the previous models can be retrieved as special cases. The model allows for arbitrary gradient scales and can describe current layers with velocity shear and large angles of magnetic field rotation. It is similar to that of Roth (1978, 1979, 1980, 1983), except that the cutoff factors are chosen in the form of error functions.

Kinetic models are of fundamental importance in understanding the structure and dynamics of transition current layers separating two magnetized plasmas with different characteristics, both in laboratory and space. In Section 2 the velocity distribution functions describing particle populations are introduced. The plasma and field boundary conditions are discussed in Section 3. Section 4 contains the

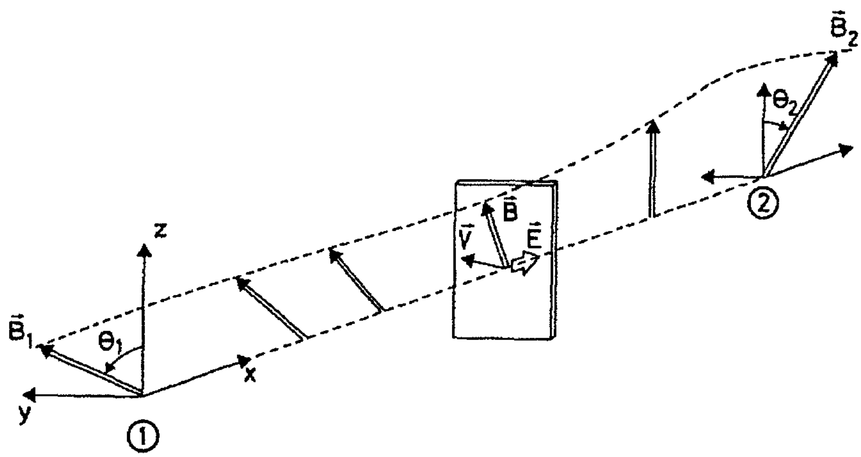

Fig. 1. Reference frame for a TD. The plane of the TD is the (y, z) plane which contains the magnetic field **B** and the velocity vector **V**. The electric field **E** is oriented along the x axis, normal to the transition. Uniform states are attained at sides 1 and 2, for large negative and positive values of x respectively.

electromagnetic field equations for the plane TD problem and a discussion of the numerical method. Armed with this kinetic framework, we first review two types of tangential discontinuities: the Harris plasma slab (Section 5) and the TD according to Sestero (Section 6). In Section 7 we simulate two observed magnetopause crossings with complex magnetic field and plasma variations. In Section 8, we show how the model can explain the microstructure of the magnetopause current layer (MCL) and its stability with respect to the excitation of large-scale tearing perturbations (Kuznetsova *et al.*, 1994; Kuznetsova and Roth, 1995). When the model is applied to the plasma sheet boundary layer in the tail or to the boundary of some plasma sheet cloud immersed in the central plasma sheet (Section 9), we obtain electric field and plasma structures which might explain the origin of discrete auroral arcs (Roth *et al.*, 1993). Because the model is able to mimic complex magnetopause transitions it also has the potential to simulate multi-species solar wind TDs observed by the interplanetary spacecraft ULYSSES (Section 10). The problems associated with the one-dimensional time-independent Vlasov approach are discussed in Section 11.

2. The Velocity Distribution Functions

The reference frame used to describe a TD is depicted in Figure 1. Electron and ion plasma species are identified by particle mass m and charge Ze, where e is the magnitude of the elementary charge ($e = 4.803 \times 10^{-10}$ statcoulomb) and Z the degree of ionization. The constants of motion of charged particles in a one-dimensional planar TD, where a scalar electric potential ϕ and a magnetic vector potential ($a_x \equiv 0, a_y, a_z$) are present, are the canonical momenta p_y and p_z and the Hamiltonian H:

$$p_y = mv_y + \frac{Zea_y}{c}, \qquad p_z = mv_z + \frac{Zea_z}{c},$$

$$H = \tfrac{1}{2}mv_x^2 + H_0(p_y, p_z)\ ,$$

where H_0 is defined by

$$H_0 = \frac{1}{2m}\left[\left(p_y - \frac{Zea_y}{c}\right)^2 + \left(p_z - \frac{Zea_z}{c}\right)^2\right] + Ze\phi\ .$$

For each species, let us consider the following velocity distribution function, which is a combination of those introduced by Roth (1978, 1979, 1980) and Lee and Kan (1979):

$$F = \eta(H, p_y, p_z)G[U_y(p_y), U_z(p_z)]\ , \tag{1}$$

with

$$\eta(H, p_y, p_z) = N\left(\frac{m}{2\pi\mathcal{T}}\right)^{3/2} \exp\left(-\frac{H}{\mathcal{T}}\right) \exp\left(-\frac{m\mathcal{U}^2}{2\mathcal{T}} + \frac{p_y\mathcal{U}_y + p_z\mathcal{U}_z}{\mathcal{T}}\right) \tag{2}$$

and the cutoff function ($C_i \geq 0$; $i = 1, \ldots, 4$)

$$\begin{aligned} G(U_y, U_z) \;=\; & \tfrac{1}{4}[C_1 \operatorname{erfc}(+U_y) \operatorname{erfc}(-U_z) + C_2 \operatorname{erfc}(-U_y) \operatorname{erfc}(-U_z) + \\ & +C_3 \operatorname{erfc}(+U_y) \operatorname{erfc}(+U_z) + C_4 \operatorname{erfc}(-U_y) \operatorname{erfc}(+U_z)], \end{aligned} \tag{3}$$

where

$$U_y = \delta_y(p_y - m\mathcal{U}_y - hp_{0y}), \qquad U_z = \delta_z(p_z - m\mathcal{U}_z - hp_{0z}), \tag{4}$$

$$\delta_y = \frac{c}{ZeB_0\rho\sqrt{l_y^2 - 1}}, \qquad \delta_z = \frac{c}{ZeB_0\rho\sqrt{l_z^2 - 1}}, \tag{5}$$

$$\rho = \frac{c\sqrt{2m\mathcal{T}}}{|Z|eB_0}. \tag{6}$$

At large distance from the TD ($x = \pm\infty$) an outer population is characterized by the Maxwellian distribution (2) with temperature $\mathcal{T}$, shifted along the v_y and v_z axes by mean velocity components $\mathcal{U}_y$ and $\mathcal{U}_z$; N is proportional to the asymptotic number density. In (4), $h = Z/|Z|$; p_{0y} and p_{0z} are two parameters controlling the separation or overlapping between outer populations originating from opposite edges of the transition. Equation (6) defines the Larmor radius ρ in a reference magnetic field $\mathbf{B}_0$.

In Equations (5), l_y and l_z are the 'normalized thicknesses' of the outer populations along the y and z directions. The 'characteristic thicknesses' of the outer populations are defined as $l_y \rho$ and $l_z \rho$; we allow different spatial extents in both coordinate directions so as to cover the case of asymmetric partial current profiles. The minimum characteristic thickness for the outer populations is the Larmor radius ($l_y = l_z = 1$). It is obtained for velocity distribution functions that are discontinuous in the (p_y,p_z) plane, e.g., distributions of the Sestero type (Sestero, 1964, 1966). These contain step functions in p_y and p_z, which are, indeed, the limiting case of cutoff function (3) when $l_y = l_z \to 1$. The use of 'erfc' cutoff functions allows smoother transitions (cf., Alpers, 1969), corresponding to a characteristic thickness larger than the Larmor radius.

When $C_1 = C_2 = C_3 = C_4 = 1$, $G(U_y, U_z) = 1$; the velocity distribution function (1)–(3) reduces to a Maxwellian shifted by the mean velocity components $\mathcal{U}_y$ and $\mathcal{U}_z$. As will be shown in Section 5, the latter distribution can describe inner populations. Furthermore, the distribution functions used in most previous TD models turn out to be special cases. In Sections 5 and 6 we will explore the relationship between the present model and those of Harris and Sestero in more detail.

The mean value $\langle w \rangle$ of a function $w(v_x, v_y, v_z)$ can be obtained from the velocity distribution function as:

$$n\langle w \rangle = \int_{-\infty}^{+\infty}\int_{-\infty}^{+\infty}\int_{-\infty}^{+\infty} w(v_x, v_y, v_z) f(v_x, v_y, v_z)\, \mathrm{d}v_x\, \mathrm{d}v_y\, \mathrm{d}v_z\ ,$$

where n is the particle number density and f the velocity distribution function in the (v_x, v_y, v_z) space. In the (H, p_y, p_z) space, f transforms into $F(H, p_y, p_z) = f[v_x(H, p_y, p_z), v_y(p_y), v_z(p_z)]$ given by Equation (1); similarly, w transforms into $W(H, p_y, p_z) = w[v_x(H, p_y, p_z), v_y(p_y), v_z(p_z)]$. Therefore:

$$\begin{aligned} n\langle w \rangle &= 2^{-1/2} m^{-5/2} \int_{-\infty}^{+\infty}\int_{-\infty}^{+\infty}\int_{H_0}^{+\infty} (H - H_0)^{-1/2} \times \\ &\times \{W[H(v_x > 0), p_y, p_z] + W[H(v_x < 0), p_y, p_z]\} \times \\ &\times F(H, p_y, p_z)\, \mathrm{d}H\, \mathrm{d}p_y\, \mathrm{d}p_z . \end{aligned} \qquad (7)$$

It is obvious that $\langle w \rangle = 0$ if w is an odd function of v_x. If $w(v_x, v_y, v_z) = v_x^r v_y^s v_z^t$, where r, s, t are non-negative integers, then the mean values $Q_{rst} = \langle v_x^r v_y^s v_z^t \rangle$ are the moments of the velocity distribution function of order $r + s + t$. In Appendix A we analytically compute the values of the most important moments, in particular:

$$\begin{aligned}
n &= Q_{000}, \\
j_y &= ZeQ_{010}, \qquad j_z = ZeQ_{001}, \\
u_y &= Q_{010}/Q_{000}, \qquad u_z = Q_{001}/Q_{000}, \\
T_x &= mQ_{200}/Q_{000}, \\
T_y &= m[Q_{020}/Q_{000} - Q_{010}^2/Q_{000}^2], \qquad T_z = m[Q_{002}/Q_{000} - Q_{001}^2/Q_{000}^2], \\
T &= (T_x + T_y + T_z)/3,
\end{aligned}$$

where n is the partial number density; j_y and j_z are the y- and z-components of the partial current density; u_y and u_z denote the y- and z-components of the partial mean velocity; and T is the partial temperature, i.e., an average of T_x, T_y, and T_z, the thermal energies along the x, y, and z axes, respectively.

3. Boundary Conditions

This section discusses the boundary conditions for the plasma and field parameters. These boundary conditions result from the uniformity of the asymptotic fields at $x = \pm\infty$. We assume that the plasma consists of s species: ℓ species originating from side 1 (left, $x = -\infty$), r species originating from side 2 (right, $x = +\infty$) and β inner populations. The asymptotic number densities must match the following boundary conditions:

$$n^{\nu_1}(-\infty) = \mathcal{N}^{\nu_1}, \quad n^{\nu_1}(+\infty) = 0, \quad \nu_1 = 1, \ldots, \ell$$

$$n^{\nu_2}(+\infty) = \mathcal{N}^{\nu_2}, \quad n^{\nu_2}(-\infty) = 0, \quad \nu_2 = 1, \ldots, r$$

$$n^{\nu_i}(\pm\infty) = 0, \quad \nu_i = 1, \ldots, \beta.$$

The asymptotic plasma ($\mathcal{N}^{\nu_1}$, $\mathcal{T}^{\nu_1}$; $\mathcal{N}^{\nu_2}$, $\mathcal{T}^{\nu_2}$) and field (B_1; B_2) parameters also satisfy the pressure balance condition:

$$\begin{aligned}
&\sum_{\nu_1=1}^{\ell} n^{\nu_1}(x)\mathcal{T}^{\nu_1} + \sum_{\nu_2=1}^{r} n^{\nu_2}(x)\mathcal{T}^{\nu_2} + \sum_{\nu_i=1}^{\beta} n^{\nu_i}(x)\mathcal{T}^{\nu_i} + \frac{B^2(x)}{8\pi} = \\
&= \sum_{\nu_1=1}^{\ell} \mathcal{N}^{\nu_1}\mathcal{T}^{\nu_1} + \frac{B_1^2}{8\pi} = \sum_{\nu_2=1}^{r} \mathcal{N}^{\nu_2}\mathcal{T}^{\nu_2} + \frac{B_2^2}{8\pi}. \qquad (8)
\end{aligned}$$

We now consider some boundary conditions which are valid on both sides of the transition. It is useful to introduce the following two coordinate systems: the first one is $(\mathbf{e}_x, \mathbf{e}_y, \mathbf{e}_z)$, where $\mathbf{e}_x$, $\mathbf{e}_y$, $\mathbf{e}_z$ are unit vectors along the (x–y–z) axes;

the second one is a local one, $(\mathbf{e}_x, \mathbf{e}_\perp, \mathbf{e}_\parallel = \mathbf{B}/B)$, obtained by a rotation around $\mathbf{e}_x$ so as to align $\mathbf{e}_z$ with $\mathbf{B}$. The asymptotic bulk velocities $\mathbf{V}_j$ are given by:

$$\mathbf{V}_j = \sum_{\nu_j} m^{\nu_j} \mathcal{N}^{\nu_j} \boldsymbol{\mathcal{U}}^{\nu_j} / \sum_{\nu_j} m^{\nu_j} \mathcal{N}^{\nu_j}, \quad j = 1, 2. \tag{9}$$

The asymptotic partial velocities $\boldsymbol{\mathcal{U}}^{\nu_j}$ are not completely arbitrary. Since the asymptotic electric fields are uniform, i.e.,

$$\mathbf{E}_j = -\frac{1}{c}\mathbf{V}_j \times \mathbf{B}_j = E_{jx}\mathbf{e}_x, \quad j = 1, 2, \tag{10}$$

the asymptotic perpendicular velocities (the electric drifts $\boldsymbol{\mathcal{U}}_\perp^{\nu_j} = \mathcal{U}_\perp^{\nu_j} \mathbf{e}_\perp = c\mathbf{E}_j \times \mathbf{B}_j / B_j^2$) are equal to the perpendicular bulk velocities ($\mathbf{V}_{j\perp} = V_{j\perp}\mathbf{e}_\perp$):

$$\boldsymbol{\mathcal{U}}_\perp^{\nu_j} = \mathbf{V}_{j\perp}, \quad \boldsymbol{\mathcal{U}}^{\nu_j} - \mathbf{V}_j = (\mathcal{U}_\parallel^{\nu_j} - V_{j\parallel})\mathbf{e}_\parallel,$$

$$\nu_1 = 1, \ldots, \ell, \quad \nu_2 = 1, \ldots, r. \tag{11}$$

From the vector product of $\boldsymbol{\mathcal{U}}^{\nu_j} = \boldsymbol{\mathcal{U}}_\perp^{\nu_j} + \mathcal{U}_\parallel^{\nu_j} \mathbf{B}_j / B_j$ with $\mathbf{B}_j$, it can be seen that:

$$\mathbf{E}_j = -\frac{1}{c}\boldsymbol{\mathcal{U}}^{\nu_j} \times \mathbf{B}_j. \tag{12}$$

The magnetic field is also uniform at $x = \mp\infty$; hence, the asymptotic vector potential is of the form:

$$a_{jy} = B_{jz}x + d_{jy}, \qquad a_{jz} = -B_{jy}x + d_{jz}, \tag{13}$$

where $\mathbf{d}_j$ does not depend on x; note that:

$$a_{j\parallel} = \mathbf{a}_j \cdot \mathbf{B}_j / B_j = \mathbf{d}_j \cdot \mathbf{B}_j / B_j = d_{j\parallel} = \text{constant}.$$

3.1. Uniform Plasma at $x = \mp\infty$

Uniform fields at $x = \mp\infty$ imply plasma neutrality and the absence of currents:

$$\sum_{\nu_j} Z^{\nu_j} \mathcal{N}^{\nu_j} = 0, \quad j = 1, 2, \tag{14}$$

$$\sum_{\nu_j} Z^{\nu_j} \mathcal{N}^{\nu_j} \mathcal{U}_\parallel^{\nu_j} = 0, \quad j = 1, 2. \tag{15}$$

From Equations (14) and (15), it can be seen that

$$\sum_{\nu_j} Z^{\nu_j} \mathcal{N}^{\nu_j} (\mathcal{U}_\parallel^{\nu_j} - V_{j\parallel}) = 0, \quad j = 1, 2. \tag{16}$$

From Equations (9) and from (11), we also have

$$\sum_{\nu_j} m^{\nu_j} \mathcal{N}^{\nu_j} (\mathcal{U}_{\parallel}^{\nu_j} - V_{j\parallel}) = 0, \quad j = 1, 2. \tag{17}$$

3.2. Boundary Conditions at $x = -\infty$

At $x = -\infty$, the function $G(\mathcal{A}_y, \mathcal{A}_z)$ defined in Appendix A by Equation (A.3) should become

$$G_1^{\nu_1} = C_{k_1}^{\nu_1} \quad \text{for} \quad \nu_1 = 1, \dots, \ell. \tag{18}$$

Here, C_{k_1} is one of the 4 constant C's in Equation (3): the one associated with the quadrant containing the asymptotic direction of a at $-\infty$. There are two possibilities to obtain $n^{\nu_2}(-\infty) = 0$: either by the choice of the cutoff factor ($G_1^{\nu_2} = 0$) or by having the exponential factor in (A.4) go to zero. The electric potential is given by

$$\phi_1 = \phi(-\infty) = (a_{1y} V_{1y} + a_{1z} V_{1z})/c, \tag{19}$$

consistent with the asymptotic electric field defined by Equation (10). From the expression for the number density (A.4), and using the information at $x = -\infty$ contained in (19), (13), (11), (18), we obtain ($\nu_1 = 1, \dots, \ell$):

$$\mathcal{N}^{\nu_1} = N^{\nu_1} C_{k_1}^{\nu_1} \exp\left[-\frac{Z^{\nu_1} e}{c \mathcal{T}^{\nu_1}} \mathbf{d}_1 \cdot (\mathbf{V}_1 - \boldsymbol{\mathcal{U}}^{\nu_1}) \right]. \tag{20}$$

Giving the constants $C_{k_1}^{\nu_1}$, the vector $\mathbf{d}_1$, the flow velocity $\mathbf{V}_1$ and the plasma parameters $\boldsymbol{\mathcal{U}}^{\nu_1}$, $\mathcal{T}^{\nu_1}$, $\mathcal{N}^{\nu_1}$, the constants N^{ν_1} can be determined from (20):

$$N^{\nu_1} = \frac{\mathcal{N}^{\nu_1}}{C_{k_1}^{\nu_1}} \exp\left[+\frac{Z^{\nu_1} e}{c \mathcal{T}^{\nu_1}} \mathbf{d}_1 \cdot (\mathbf{V}_1 - \boldsymbol{\mathcal{U}}^{\nu_1}) \right]. \tag{21}$$

In summary, at $x = -\infty$, the boundary conditions for the plasma number densities and velocities ($\nu_1 = 1, \dots, \ell$) must meet Equations (14), (16), and (17) for $j = 1$. The electric potential is given by Equation (19), while the vector potential can be found from (13, $j = 1$). The parameters N^{ν_1} are obtained from (21). A transition where the partial velocities at $-\infty$ are all different is given in Section 10 for a solar wind TD containing helium ions.

3.3. Boundary Conditions at $x = +\infty$

At $x = +\infty$, the function $G(\mathcal{A}_y, \mathcal{A}_z)$ defined by Equation (A.3) has the value:

$$G_2^{\nu_2} = C_{k_2}^{\nu_2} \quad \text{for} \quad \nu_2 = 1, \dots, r. \tag{22}$$

C_{k_2} is one of the constants in Equation (3), identifying the quadrant with the asymptotic direction of a at $+\infty$. Note that $n^{\nu_1}(+\infty) = 0$ can be obtained by

$G_2^{\nu_1} = 0$ or by a vanishing exponent in (A.4). From (A.4) the number densities ($\nu_2 = 1, \ldots, r$) at $x = +\infty$ are:

$$\mathcal{N}^{\nu_2} = N^{\nu_2} C_{k_2}^{\nu_2} \exp\left[-\frac{Z^{\nu_2} e}{\mathcal{T}^{\nu_2}}\left(\phi_2 - \frac{a_{2y}\mathcal{U}_{2y}^{\nu_2} + a_{2z}\mathcal{U}_{2z}^{\nu_2}}{c}\right)\right]. \tag{23}$$

At $x = +\infty$, the electric potential is:

$$\phi_2 = \phi(+\infty) = (a_{2y}V_{2y} + a_{2z}V_{2z})/c + \psi_2, \tag{24}$$

where ψ_2 is a constant. From Equations (23), (24), (13) and (11), the number densities ($\nu_2 = 1, \ldots, r$) can be written as:

$$\mathcal{N}^{\nu_2} = N^{\nu_2} C_{k_2}^{\nu_2} \exp\left\{-\frac{Z^{\nu_2} e}{\mathcal{T}^{\nu_2}}\left[\psi_2 + \frac{1}{c}\mathbf{d}_2 \cdot (\mathbf{V}_2 - \boldsymbol{\mathcal{U}}^{\nu_2})\right]\right\}, \tag{25}$$

where N^{ν_2}, ψ_2 and $\mathbf{d}_2$ are unknown parameters.

In order to obtain finite number densities at $x = +\infty$, the exponential term in (23) must remain bounded. In this case, the number densities have the form given by (25), where $\mathbf{d}_2$ is a constant vector such that $d_{2\|} = a_{2\|}$ (in this case the field $\mathbf{B}_2$ at $x = +\infty$ is uniform, see (13)). This implies that all partial velocities at $x = +\infty$ have the same perpendicular components in order that the electric field be uniform (see Equations (11)–(12)). Because the orientation of the magnetic field at $x = +\infty$ is unknown, the simplest way to obtain a satisfactory solution is to choose

$$\boldsymbol{\mathcal{U}}^{\nu_2} = \mathbf{V}_2 \quad \text{for } \nu_2 = 1, \ldots, r. \tag{26}$$

At $x = +\infty$, the plasma must meet Equation (14, $j = 2$), i.e., a charge neutrality condition. From (26), it can be seen that the conditions for the absence of field-aligned current (16) and mass flow (17) are both satisfied. From (25), we find that

$$\mathcal{N}^{\nu_2} = N^{\nu_2} C_{k_2}^{\nu_2} \exp\left(-\frac{Z^{\nu_2} e}{\mathcal{T}^{\nu_2}}\psi_2\right). \tag{27}$$

From (27), it can be seen that either ψ_2 or one of the set $N^{\nu_2=1}, \ldots, N^{\nu_2=r}$ is arbitrary. If ψ_2 is given,

$$N^{\nu_2} = \frac{\mathcal{N}^{\nu_2}}{C_{k_2}^{\nu_2}} \exp\left(+\frac{Z^{\nu_2} e}{\mathcal{T}^{\nu_2}}\psi_2\right) \quad \text{for } \nu_2 = 1, \ldots, r. \tag{28}$$

If, on the other hand, the value N^{j_2} is given for species j_2, we have:

$$\begin{aligned} \psi_2 &= -\frac{\mathcal{T}^{j_2}}{Z^{j_2} e} \ln\left(\frac{\mathcal{N}^{j_2}}{N^{j_2} C_{k_2}^{j_2}}\right), \\ N^{\nu_2} &= \frac{\mathcal{N}^{\nu_2}}{C_{k_2}^{\nu_2}} \left[\frac{N^{j_2} C_{k_2}^{j_2}}{\mathcal{N}^{j_2}}\right]^{Z^{\nu_2}\mathcal{T}^{j_2}/Z^{j_2}\mathcal{T}^{\nu_2}}, \quad \nu_2 = 1, \ldots, j_2 - 1; j_2 + 1, \ldots, r. \end{aligned} \tag{29}$$

4. The Electromagnetic Field Structure

In this section we derive the electromagnetic field equations. Reference values for all physical quantities are introduced in Appendix B. Choosing such a set of reference values allows a dimensionless formulation of the electromagnetic field equations. In particular, we select a reference particle with mass m_0, degree of ionization Z_0, and thermal energy T_0; and a reference magnetic field B_0. The reference length ρ_0 is the gyroradius of the reference particle in a uniform magnetic field with the reference intensity B_0. The reference velocity $v_0 = \sqrt{2T_0/m_0}$ is the perpendicular thermal velocity of the reference particle population.

The characteristic thicknesses $l_{y,z}\rho$ of a particular species are defined in units of the reference length (ρ_0). The corresponding dimensionless thicknesses are:

$$L_y = l_y\rho/\rho_0, \quad L_z = l_z\rho/\rho_0.$$

The form of the dimensionless field equations is affected only by the fact that the dimensionless velocity of light (c^*) and elementary charge (e^*) must be used:

$$c^* = c/v_0, \quad e^* = c/|Z_0|v_0.$$

In the sequel, the * superscript is dropped, unless to identify dimensionless quantities whenever confusion might arise.

The electromagnetic field is described by the electric potential ϕ, for which

$$E_x(x) = -\frac{\mathrm{d}\phi}{\mathrm{d}x},$$

and the magnetic vector potential components a_y and a_z, whose curl is:

$$\frac{\mathrm{d}a_y}{\mathrm{d}x} = B_z, \quad \frac{\mathrm{d}a_z}{\mathrm{d}x} = -B_y. \tag{30}$$

The vector potential is computed from Ampère's law:

$$\frac{\mathrm{d}^2a_y}{\mathrm{d}x^2} = -\frac{4\pi}{c}J_y, \quad \frac{\mathrm{d}^2a_z}{\mathrm{d}x^2} = -\frac{4\pi}{c}J_z, \tag{31}$$

while Poisson's equation must be solved in order to find the electric potential. The latter equation, however, can be replaced by the charge neutrality equation (see Roth *et al.*, 1990):

$$\sum_{\nu=1}^{s} Z^\nu n^\nu(x) = 0, \tag{32}$$

where s is the total number of plasma species ($s = \ell + \beta + r$).

By calculating the first and second derivatives of (32) with respect to x, with $n^\nu(\phi(x), a_y(x), a_z(x))$, we can obtain expressions for the electric field E_x and charge density q, as functions of $\phi(x)$, $a_y(x)$ and $a_z(x)$. These expressions can be found in Appendix C.

The numerical solution of the electromagnetic structure of the TD becomes straightforward by reformulating the field Equations (30) and (31) as a nonlinear system of ordinary first-order differential equations for $a_y(x)$, $a_z(x)$, $B_y(x)$, and $B_z(x)$; coupled with the quasi-neutrality Equation (32). This system of ordinary differential equations is solved numerically by means of Hamming's predictor-corrector scheme (Ralston and Wilf, 1965); the nonlinear algebraic quasi-neutrality equation is solved by the Newton-Raphson method (Press *et al.*, 1986). In the remainder of this paper we will review several types of TD based on computations with this numerical scheme.

5. Harris' Plasma Slab

The Harris model (Harris, 1962) is of particular historic importance, as it was one of the first to explain a reversal of the magnetic field. The physical configuration is simple: the model describes a neutral plasma slab containing only inner particles; no particles are present on either side of the slab. The magnetic field vector always lies in the z-direction; therefore, $a_z(x) \equiv 0$, and p_z drops out of the equations of motion. The boundary conditions are ($B_R > 0$):

$$B_y(x) = 0, \quad B_z(0) = 0, \quad B_{1z} = -B_R, \quad B_{2z} = +B_R, \tag{33}$$

which corresponds to $C_1 = C_2 = C_3 = C_4 = 1$ and

$$\mathcal{U}_y = \mathcal{U}_H = -2c\mathcal{T}/(ZeB_R\mathcal{L}_H), \quad \mathcal{U}_z = 0; \tag{34}$$

$\mathcal{L}_H$ is the Harris thickness (see below). In this case $G(p_y, p_z) = 1$, and

$$\eta(H, p_y) = N\left(\frac{m}{2\pi\mathcal{T}}\right)^{3/2} \exp\left(-\frac{H}{\mathcal{T}}\right) \exp\left(-\frac{m\mathcal{U}_H^2}{2\mathcal{T}} + \frac{\mathcal{U}_H p_y}{\mathcal{T}}\right). \tag{35}$$

This distribution is, in fact, a Maxwellian shifted by the drift velocity $\mathcal{U}_H$:

$$\eta(x, v_x, v_y, v_z) = n(x)\left(\frac{m}{2\pi\mathcal{T}}\right)^{3/2} \exp\left\{-\frac{m}{2\mathcal{T}}[v_x^2 + (v_y - \mathcal{U}_H)^2 + v_z^2]\right\},$$

with number density distribution:

$$n(x) = n(\phi(x), a_y(x)) = N \exp\left[-\frac{Ze}{\mathcal{T}}\left(\phi - \frac{\mathcal{U}_H a_y}{c}\right)\right].$$

In an isothermal plasma containing electrons ($Z = -1$) and protons ($Z = 1$), the slab is exactly charge neutral ($\phi \equiv 0$) when $\mathcal{U}_H^- = -\mathcal{U}_H^+ = 2c\mathcal{T}/(eB_R\mathcal{L}_H)$ (one

TABLE II
The Harris model (cf., Harris, 1962, Figure 1)

Reference parameters and boundary conditions										
	$\mathcal{T}_0$ eV	B_0 nT	k_1	k_2	ψ_2 V	x_0^*	B_1 nT	θ_0 °	a_{0y}^*	a_{0z}^*
Protons	1000	60	2	4	0	0	60	0	0	0

Inner populations						
	N cm^{-3}	$\mathcal{T}$ eV	$\mathcal{U}_y$ km s^{-1}	$\mathcal{U}_z$ km s^{-1}	C_i	$\mathcal{L}_H/\rho_0$
Electrons	4.47	1000	146	0	1 1 1 1	3
Protons	4.47	1000	−146	0	1 1 1 1	3

can always transform to a reference frame that moves along the y axis, in which this condition is satisfied). Analytically solving

$$\frac{\mathrm{d}^2 a_y}{\mathrm{d}x^2} = \frac{8\pi e N \mathcal{U}_H^-}{c} \exp\left(-\frac{e\mathcal{U}_H^- a_y(x)}{c\mathcal{T}}\right)$$

with boundary conditions

$$\frac{\mathrm{d}a_y}{\mathrm{d}x}(0) = 0, \quad a_y(\pm\infty) = \pm B_R x, \tag{36}$$

reveals that:

$$a_y(x) = \frac{2\mathcal{T} c}{e\mathcal{U}_H^-} \ln\cosh(x/\mathcal{L}_H),$$

$$B_z(x) = \frac{\mathrm{d}a_y}{\mathrm{d}x} = B_R \tanh(x/\mathcal{L}_H), \quad n(x) = N/\cosh^2(x/\mathcal{L}_H), \tag{37}$$

$$\mathcal{L}_H = \frac{c}{\mathcal{U}_H^-}\mathcal{L}_D, \quad \mathcal{L}_D = \left(\frac{\mathcal{T}}{4\pi N e^2}\right)^{1/2};$$

$\mathcal{L}_D$ is the Debye length, and $\mathcal{L}_H$ is the half-thickness of the slab. The Harris thickness $\mathcal{L}_H$ can approach $\mathcal{L}_D$ in the limiting case $\mathcal{U}_H \to c$.

We have computed the structure of the slab for the case summarized in Table II. The reference particle is a 1 keV proton, the length scale being its Larmor radius ($\rho_0 \approx 75$ km) in the 60 nT magnetic field at $-\infty$. Electrons and protons have the

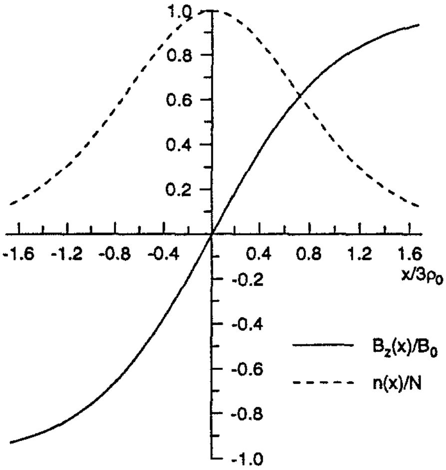

Fig. 2. The Harris model: magnetic field reversal and the number density of the inner particles (cf., Harris, 1962, Figure 1).

same temperature $\mathcal{T} = \mathcal{T}^{\nu_i=1} = \mathcal{T}^{\nu_i=2} = 1$ keV. The value of N is obtained from the pressure balance Equation (8):

$$\frac{B_1^2}{8\pi} = N^{\nu_i=1}\mathcal{T}^{\nu_i=1} + N^{\nu_i=2}\mathcal{T}^{\nu_i=2} = 2N\mathcal{T}.$$

Plasma neutrality implies that

$$N^{\nu_i=1} = N^{\nu_i=2} = n^{\nu_i=1}(x^* = 0) = n^{\nu_i=2}(x^* = 0) = N.$$

The drift velocities have been computed from Equation (34), with $\mathcal{L}_H = 3\rho_0$. The numerical integration starts from $x_0^* = 0$ and proceeds towards $-\infty$ up to the turning point x_t^*, where the total current density becomes negligibly small, and then back towards $+\infty$. The values of k_1, k_2, and θ_0 satisfy the boundary conditions (36) (θ_0 refers to the angle between $\mathbf{B}(0)$ and the z-axis). The Newton–Raphson scheme finds the true value of $\phi(x^* = 0)$ before the integration starts; here, the correct value $\phi(x^* = 0) = 0$ is provided as initial guess.

Figure 2 illustrates the antisymmetric magnetic field reversal, as well as the symmetry of the number density profile, as dictated by Equations (37). Note that a B_z reversal can also be obtained with a particle distribution different from that of Harris.

The 'modified Harris model' is an extension that includes a uniform B_y component $B_y(x) \equiv B_{y0}$:

$$\mathbf{B} = B_z(x)\mathbf{e}_z + B_{y0}\mathbf{e}_y, \quad a_z(x) = -B_{y0}x + a_z(0) \tag{38}$$

where $\mathbf{e}_y$ and $\mathbf{e}_z$ are unit vectors along the y and z axes, respectively. The introduction of a constant B_y does not influence the conservation of H and p_y; the

TABLE III

The Sestero model (cf., Sestero, 1966, Figure 1)

Reference parameters and boundary conditions									
	$\mathcal{T}_0$ eV	B_0 nT	k_1 k_2	ψ_2 V	x_0^*	B_1 nT	θ_0 °	a_{0y}^*	a_{0z}^*
Electrons	100	10	1 2	0	0	13.5	0	0	0

Plasma populations									
	N cm^{-3}	$\mathcal{T}$ eV	$\mathcal{U}_y$ km s^{-1}	$\mathcal{U}_z$ km s^{-1}	C_i	L_y	L_z	p_{0y}^*	p_{0z}^*
Outer left populations									
Electrons	2.48	100	0	0	1 1 1 1	–	–	–	–
Protons	2.48	100	0	0	1 0 1 0	42.9	–	0	–
Outer right populations									
Electrons	2.48	100	-119	0	1 1 1 1	–	–	–	–
Protons	2.48	100	-119	0	0 1 0 1	42.9	–	0	–

particle distribution is still given by Equation (35) and the $B_z(x)$ component and density profiles are described by Equations (37). The modified Harris model is often encountered in kinetic studies of magnetopause stability (Galeev *et al.*, 1986). Indeed, this equilibrium describes the main property of the magnetopause: the rotation of the magnetic field vector across the layer. The stability analysis by Galeev *et al.* (1986) is, however, not appropriate for the case of nearly opposite directions of magnetosheath and magnetospheric magnetic fields (for $|B_{y0}| \ll B_R$) when configuration (38) tends to the one-dimensional 'neutral sheet' limit. Although many magnetopause crossings are characterized by a magnetic field rotation close to 180° (e.g., Berchem and Russell, 1982b), one-dimensional neutral sheets ($B_{y0} \to 0$) as well as layers with a constant or nearly constant value of B_y are seldom observed. What is actually observed is a systematic variation of both B_y and B_z as the satellite passes through the magnetopause, while the quantity $B_y^2 + B_z^2$ remains approximately constant even when the magnetic field rotation tends to 180°. Sections 7 and 8 describe realistic magnetopause equilibria and present results of a stability analysis which generalizes the approach by Galeev *et al.* (1986).

6. Sestero's TD Model

The Sestero model (Sestero, 1966) describes the transition between two plasmas on either side of a TD, each consisting of electron and proton populations only ($s = 4$, $\ell = r = 2$). However, no inner populations confined in the transition layer are considered. The magnetic field remains parallel to the z axis, like in the Harris model, but a velocity shear perpendicular to the magnetic field (along the y axis) may be present. When the plasma state is assumed to be identical on both sides of the layer, the structure of the TD is only controlled by the flow shear. A previous paper by Sestero (1964) was limited to a class of TDs involving no shearing (with the plasma macroscopically at rest on both sides of the discontinuity).

In this section, it is shown that Sestero's TD can be retrieved from the generalized model. To illustrate this assertion, the ion-dominated layer in Sestero (1966, Figure 1) is simulated here (see Table III). The length scale adopted here is the electron gyroradius in an arbitrary magnetic field of 10 nT, rather than the electron skin depth used in Sestero (1966). To single out the effect of the velocity shear, Sestero had prescribed identical asymptotic number densities and temperatures. In Table III, the temperatures of both electrons and protons are arbitrarily chosen equal to 100 eV, but the asymptotic number densities have been computed so that the reference length (the electron gyroradius) is the same as the electron skin depth. Therefore, the results obtained by Sestero (1966) can be directly compared with the simulation of this section.

The velocity shear V_{2y} is -118.619 km s^{-1}, which corresponds to Sestero's value: $V_{2y}^* = -0.02$. At the center of the transition $a_{0y}^* = a_{0z}^* = 0$ and $B(0) = B_0$. The magnetic field B_1 at $x = -\infty$ is computed from the pressure balance condition. Because of the sign of V_{2y} there is no need for a cutoff factor in the electron velocity distribution functions. The latter are Maxwellians (for the electron population originating from the right of the layer, it is shifted along the v_y axis by the velocity shear V_{2y}) but yet have the desired asymptotic behavior: if $V_{2y} < 0$ and $B_z > 0$, the number density of the electron population originating from the left (right) tends to zero at $x = +\infty$ ($x = -\infty$) like the exponential term in (A.4). In this model the sign of the shear flow determines the nature of the transition: it is an ion-dominated layer when $V_{2y} < 0$, and an electron-dominated one when $V_{2y} > 0$.

The ion distribution function in the (p_y, p_z) plane is a step function in p_y (for the ion population originating from $x = +\infty$ it is centered on $p_y = m^+V_{2y}$). Therefore, the values of L_y^+ are equal to ρ^+/ρ_0, corresponding to $l_y^+ = 1$. The relative electric potential difference ψ_2 was chosen to be zero in this simulation.

Figure 3 illustrates the structure of the Sestero TD; it is identical to the figure in Sestero (1966, Figure 1), except for the scaling of the electrical potential. The magnetic field remains parallel to the z-axis; this results from the choice of the constants C. In the phase space, the ions originating from $x = -\infty$ are located to the left of the line $p_y = V_{2y}$, while those originating from $x = +\infty$ are found to the right of this line. This distribution is symmetrical with respect to the p_y axis and therefore cannot generate any j_z^+ current.

Note from Equation (B.1) that V_{2y}^* is of the order of the ion thermal speed. Taking larger negative values for V_{2y}^* leads to extreme variations of the density and the magnetic field, and eventually produces a set of oscillatory solutions, with the magnetic field periodically assuming both positive and negative values (Sestero, 1966). The latter solutions do not satisfy the desired asymptotic conditions at infinity, and therefore are disregarded. The thickness of the TD illustrated in Figure 3 is of the order of the ion Larmor radius. It was shown by Sestero (1966) that the maximum amount of velocity shear that can be supported by the plasma over the distance of an ion (electron) Larmor radius – in an ion-dominated layer (electron-dominated layer) – is given by the ion (electron) thermal speed, if the motion is in the direction indicated by the negative (positive) sign of V_{2y}.

Some heuristic remarks were given by Sestero concerning the reasons for the peculiar asymmetry that was found in the solutions' behavior with respect to the sign of V_{2y}, for a fixed sign of the asymptotic magnetic field: by fixing the sign of V_{2y}, one determines the sign of the inductive electric fields in the moving section of the plasma. It is expected that the orbits of ions and electrons will be affected differently in the two cases.

The above conclusions concerning the minimum width of the layers and the maximum change in the macroscopic velocity that the plasma can support over such minimum distance can be made plausible by simple arguments (Sestero, 1966). If $\mathcal{L}$, J, and δB are representative values of the thickness, current density, and total change in the magnetic field, respectively, then

$$\delta B = (4\pi/c)J\mathcal{L}.$$

Considering changes of the magnetic pressure of the order of the plasma pressure, i.e., $\delta(B^2/8\pi) = (4\pi)^{-1}B\delta B \approx 2\mathcal{N}\mathcal{T}$, it can be seen that:

$$\mathcal{L} \approx 2c\mathcal{N}\mathcal{T}/(BJ).$$

Considering that $J \leq e\mathcal{N}(2\mathcal{T}/m^{\pm})^{1/2}$, with the superscripts $^+$ and $^-$ referring in this order to the ion-dominated and electron-dominated cases, it can be deduced that

$$\mathcal{L} \geq \rho^{\pm}. \tag{39}$$

If, in an ion-dominated layer, the average distance traveled by ions that cross into the transition region from near the border of that side of the plasma which is at rest, is as small as an ion Larmor radius, the gain of kinetic energy can be at most of the order of the initial kinetic energy itself. Therefore, $eE\mathcal{L} \leq \mathcal{T}$. But the electric field can be estimated in terms of its asymptotic value $E \approx (V_{2y}/c)B$. Therefore, $V_{2y} \leq c\mathcal{T}/(eB\mathcal{L})$, or from (39):

$$V_{2y} \leq (1/2)(2\mathcal{T}/m^+)^{1/2}.$$

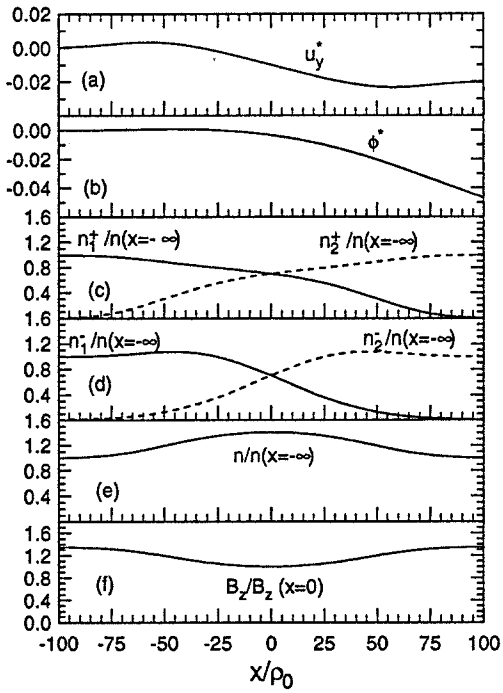

Fig. 3. The Sestero model: (a) the (normalized) perpendicular bulk velocity; (b) the (normalized) electric potential; (c) the proton number densities; (d) the electron number densities; (e) the total number density; (f) the magnetic field.

A similar result holds for the case of an electron-dominated layer. The computation of explicit solutions by Sestero demonstrates that ion-dominated or electron-dominated profiles do exist and that they can be as sharp as the *a priori* estimates (39) allow them to be. Results of hybrid simulations, however, do not show gradient scales as small as the electron gyroradius (Cargill and Eastman, 1991). Such small scales give rise to current-driven micro-instabilities, which result in a subsequent widening of the layer.

7. Simulations of the Magnetopause Structure

Many equilibrium Vlasov models of TDs have been used to describe specific features of the magnetopause structure (see Table I). A powerful model is needed if one wants to reproduce the magnetopause characteristics observed during an actual satellite crossing. In this section we present simulations of two magnetopause crossings:

– In the first simulation, we reproduce a magnetopause crossing showing maximum magnetic field intensity at the center of the transition. This case was also simulated by Lee and Kan (1979).

TABLE IV
The Lee and Kan model

Reference parameters and boundary conditions									
	$\mathcal{T}_0$ eV	B_0 nT	k_1 k_2	ψ_2 V	x_0^*	B_1 nT	θ_0 °	a_{0y}^*	a_{0z}^*
Protons	1000	50	1 4	0	−8.08	46.1	−49.4	−7	+7

Plasma populations									
	N cm^{-3}	$\mathcal{T}$ eV	$\mathcal{U}_y$ km s^{-1}	$\mathcal{U}_z$ km s^{-1}	C_i	L_y	L_z	p_{0y}^*	p_{0z}^*
Outer left populations									
Electrons	6.2	30	0	0	1 0 0 0	0.81	0.81	−1.4	0
Protons	6.2	400	0	0	1 0 0 0	2.53	2.53	−1.4	0
Outer right populations									
Electrons	21.7	20	0	0	0 1 1 1	0.66	0.66	0	0
Protons	21.7	200	0	0	0 1 1 1	1.79	1.79	0	0

– The second simulation models a magnetopause crossing observed by the ISEE-1 satellite, with shears in the magnetic field and the plasma velocity.

7.1. The Lee and Kan TD magnetopause model

Lee and Kan (1979) elaborate a kinetic model of the tangential magnetopause structure (see Table I). We show that this model is a particular case of our general one, by illustrating the role of the parameters p_{0y} and p_{0z}. By choosing non-zero values for these parameters Lee and Kan (1979, Figure 4) were able to describe a magnetopause transition where the magnetic field intensity is enhanced inside the transition layer. This feature was observed during the November 5, 1977, ISEE-1 magnetopause crossing (Russell and Elphic, 1978; Paschmann *et al.*, 1978). All the features of Lee and Kan (1979, Figure 4) are reproduced in Figure 4 using our general model with boundary conditions and plasma populations given in Table IV. Lee and Kan assumed no velocity shear between the magnetospheric and the magnetosheath plasmas in this example ($\mathbf{V}_1 = \mathbf{V}_2 = 0$).

Note that inner particles are absent in this example and the angle of magnetic field rotation is therefore small (15°). The choice of p_{0y} and p_{0z} reflects that there is less interpenetration between the magnetospheric and the magnetosheath plasmas.

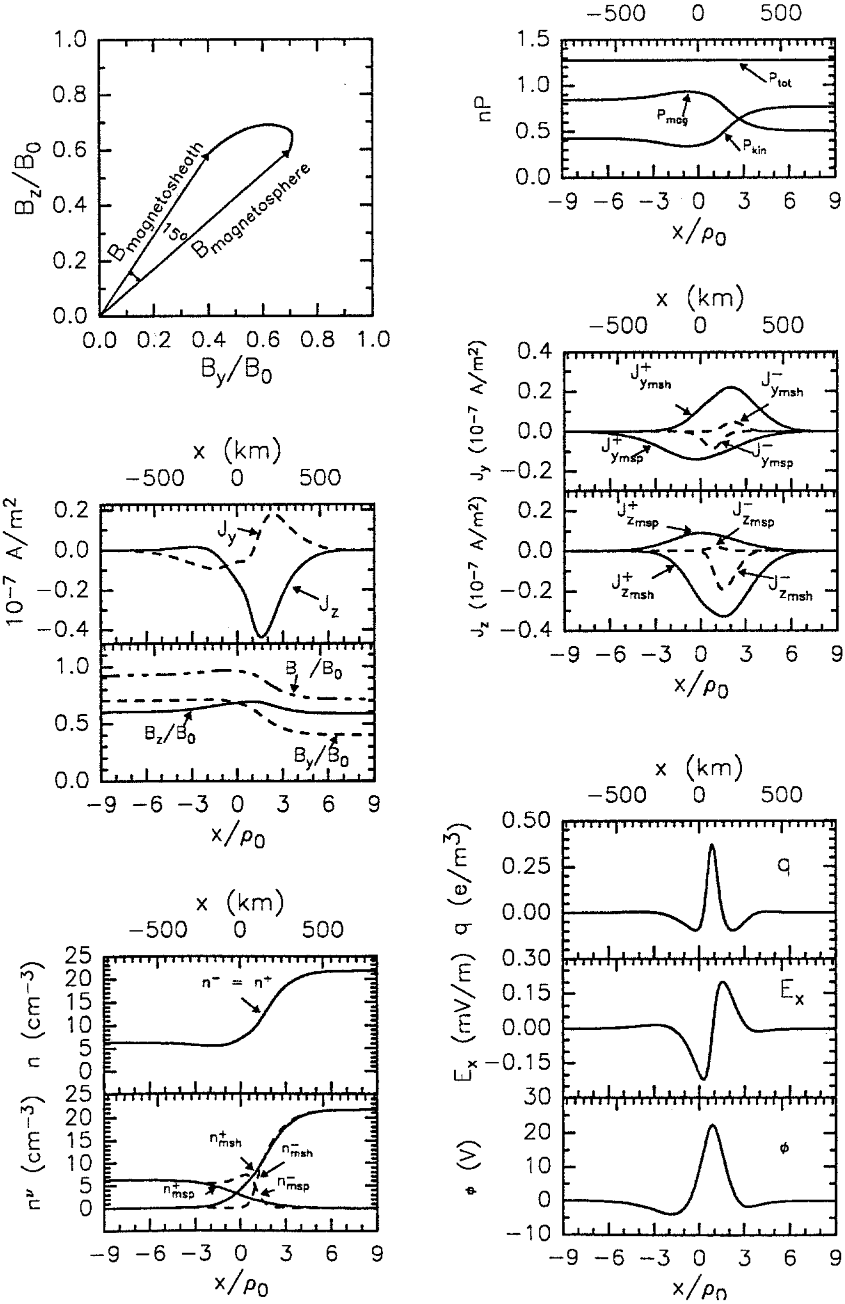

Fig. 4. TD structure with maximum B inside the magnetopause. This figure corresponds to Lee and Kan (1979, Figure 4).

7.2. A MAGNETOPAUSE CROSSING BY ISEE-1

A test for the maturity of the model consists in simulating TD transitions observed by spacecraft *in situ*. In this subsection we do so for a magnetopause crossing by the ISEE-1 spacecraft on August 17, 1978. The crossing occurs between 01:41:50 UT and 01:42:40 UT. High time-resolution measurements of the magnetic field (courtesy: C. T. Russell, UCLA) are shown in Figure 5. A minimum variance analysis was carried out (courtesy: J. Berchem, UCLA) to compute the B_y and B_z components tangential to the discontinuity plane. Corresponding plasma data were deduced from measurements by the LEPEDEA experiment (courtesy: L. Frank and T. E. Eastman, University of Iowa). These plasma data were used to construct Table V. The values of L_y and L_z for each proton population correspond to $l_y = l_z = 1$, that is, $L_y = L_z = \rho/\rho_0$ (velocity distribution functions of Sestero type). The velocity distribution function of each electron population is a shifted Maxwellian, since for these populations $C_k = 1$ $(k = 1, \ldots, 4)$. Note that there are no inner populations in this simulation. Except for the small-scale time-dependent fluctuations of the magnetic field, the experimental profiles of B_y and B_z illustrated in Figure 5 are well reproduced in Figure 6. Note in particular that the observed slow decrease of B_z is explained by the presence of an extended $j_y^{\nu_2=4}$ current carried by magnetospheric protons of high energy (13 900 eV). The electric current density, number density and temperature distributions are illustrated in Figure 7. Figure 8 displays the electric structure and the plasma bulk velocity.

8. Structure and Stability of the Magnetopause

Stability is an important topic in the study of equilibrium models. This section will be devoted to the structure and stability of the magnetopause in the framework of our general equilibrium model for TDs; it was not meant to be a complete review on this topic.

The first electric field evidence of plasma wave turbulence at the dayside magnetopause was obtained by Gurnett *et al.* (1979) who reported burstly low-frequency ($<$100 Hz) electric and magnetic fluctuations. Gary and Eastman (1979) suggested that the lower-hybrid drift instability (Davidson *et al.*, 1977; Huba *et al.*, 1978) could directly account for the observed fluctuations and that the mode should be driven by small-scale density gradients. Roth (1979, 1980) suggested that current-driven lower hybrid instabilities – like the modified two-stream instability (McBride *et al.*, 1972; Wu *et al.*, 1983) or the lower-hybrid drift instability – can be expected to relax the strong gradients in both the plasma density and flows that one is able to reproduce in TDs with small gradient scales. Both instabilities contribute to a wave spectrum near the lower-hybrid frequency.

Observations of possible tearing-produced magnetic islands in both laboratory terrella experiments (Dubinin *et al.*, 1980) and space observations at the Earth and

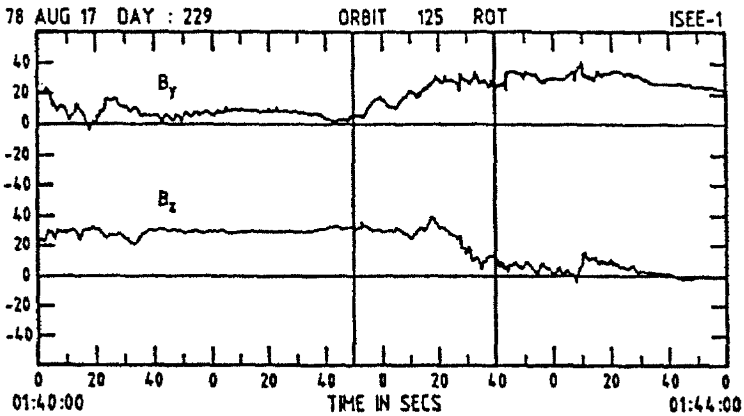

Fig. 5. High time-resolution magnetic field measurements by ISEE-1, during the August 17, 1978 magnetopause crossing (courtesy: C. T. Russell, UCLA).

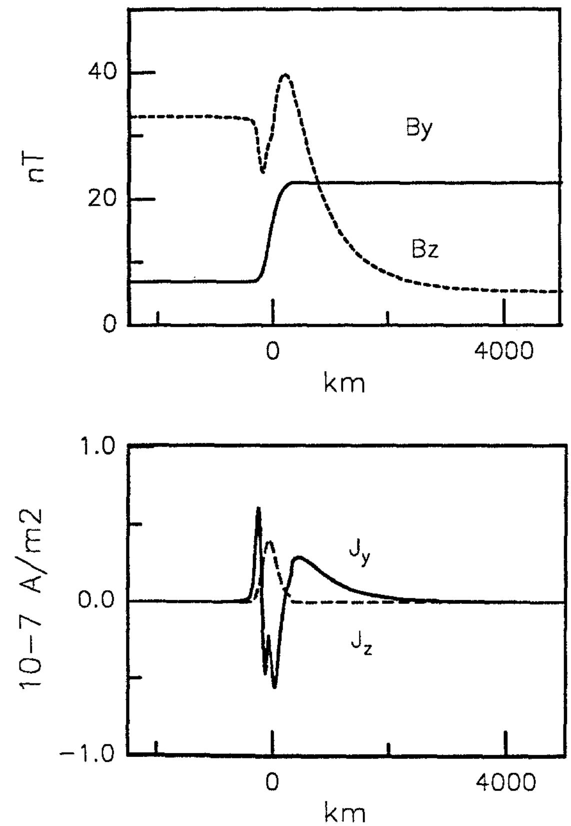

Fig. 6. Simulation of an ISEE-1 magnetopause crossing: field and current profiles.

TABLE V

Simulation of an ISEE-1 magnetopause crossing

Reference parameters and boundary conditions									
	T_0 eV	B_0 nT	k_1 k_2	ψ_2 V	x_0^*	B_1 nT	θ_0 °	a_{0y}^*	a_{0z}^*
Protons	160	33.7	1 4	0	−62.2	33.7	348.1	−57.6	38.1
Plasma populations									
	N cm^{-3}	T eV	U_y km s^{-1}	U_z km s^{-1}	C_i	L_y	L_z	p_{0y}^*	p_{0z}^*
Outer left populations									
Cold electrons	12.8	7	−44	−141	1 1 1 1	–	–	–	–
Cold protons	18.5	160	−44	−141	1 0 1 0	1	–	0	–
Hot electrons	6.6	45	−44	−141	1 1 1 1	–	–	–	–
Hot protons	0.9	1180	−44	−141	1 0 1 0	2.72	–	0.6	–
Outer right populations									
Cold electrons	0.78	30	−142	−102	1 1 1 1	–	–	–	–
Cold protons	0.51	545	−142	−102	0 1 0 1	1.85	–	0.6	–
Hot electrons	0.12	1500	−142	−102	1 1 1 1	–	–	–	–
Hot protons	0.39	13900	−142	−102	0 1 0 1	9.32	–	11.5	–

Jupiter magnetopauses (Greenly and Sonnerup, 1981) suggest the possible occurrence of the tearing mode instability. The linear and nonlinear dynamics of the collisionless drift tearing mode has been thoroughly investigated by a number of authors (e.g., Galeev and Zelenyi, 1977; Drake and Lee, 1977; Coppi *et al.*, 1979; Quest and Coroniti, 1981a, b; Kuznetsova and Zelenyi, 1985, 1990a, b; Gladd, 1990). A stochastic percolation model based on these studies has been suggested by Galeev *et al.* (1986). In this section we will illustrate two magnetopause equilibrium models and discuss their stability with respect to spontaneous excitation of collisionless tearing perturbations:

– A combination of the Harris and Sestero models to illustrate the effects of the relative flow velocity on the structure and stability of a MCL with nearly antiparallel asymptotic magnetic fields (Kuznetsova *et al.*, 1994).

– A tractable version (i.e., with a minimum number of free parameters) of our general TD model to explore the effects of asymmetrical magnetic field profiles. In the latter simulation, the velocity shear is neglected (Kuznetsova and Roth, 1995).

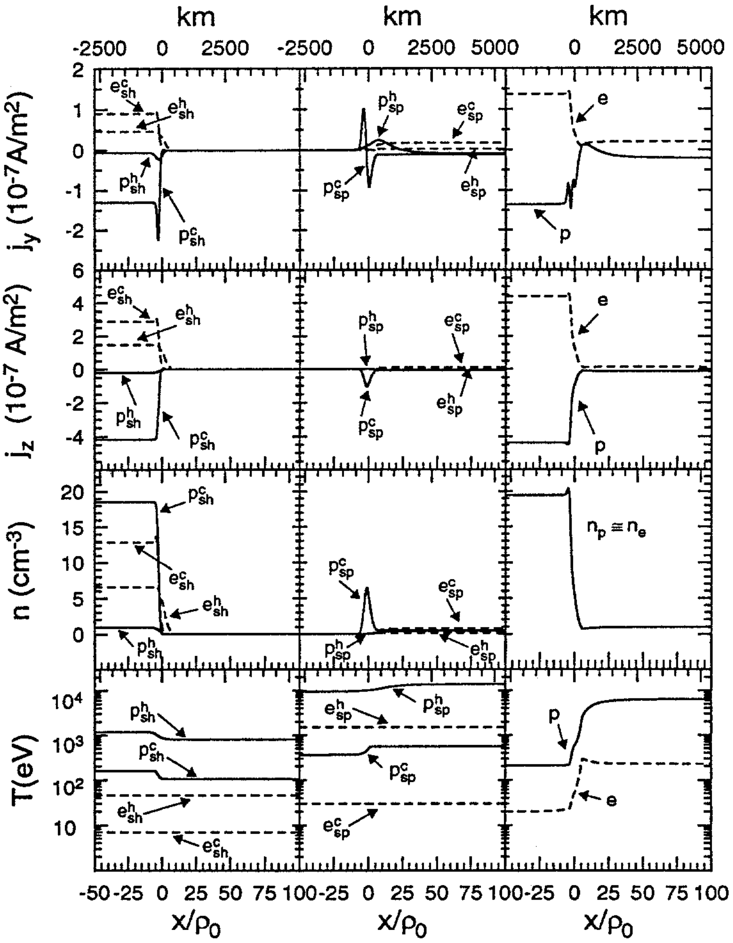

Fig. 7. Simulation of an ISEE magnetopause crossing. Labels e and p refer to electron and proton populations. Subscript sh identifies particles originating in the magnetosheath, while sp refers to particles from the magnetosphere. Superscripts c and h refer to cold and hot populations.

In both models periodic perturbations of vector and scalar potentials are described by small variations $\tilde{A}_y$,$\tilde{A}_z$, $\tilde{\varphi}$ $\sim$ exp$(ik_z z+ik_y y)$ superposed on the equilibrium vector and scalar potentials a_y, a_z, and ϕ: A_y=a_y+$\tilde{A}_y$, A_z=a_z+$\tilde{A}_z$, Φ=ϕ+$\tilde{\varphi}$. Taking into account the approximate gauge condition $\mathbf{k} \cdot \mathbf{A} = 0$ it is convenient to introduce the scalar quantity A=$A_{\|}$=$(k_z\tilde{A}_y- k_y\tilde{A}_z)/k$, which corresponds to the component of the vector potential parallel to the local direction of the magnetic field near the so-called singular magnetic surface x_s, where $\mathbf{k}\cdot\mathbf{B}(x_s)$=0 (i.e., $B_z(x_s)/B_y(x_s)$=$-k_y/k_z$).

We assume that adiabatically perturbed electric current and number densities can be expressed as functions of Φ, A_y, and A_z, and expanded in Taylor series for $\tilde{A}_y \ll a_y$, $\tilde{A}_z \ll a_z$, $\tilde{\varphi} \ll \phi$. The linearized Maxwell equations and quasi-

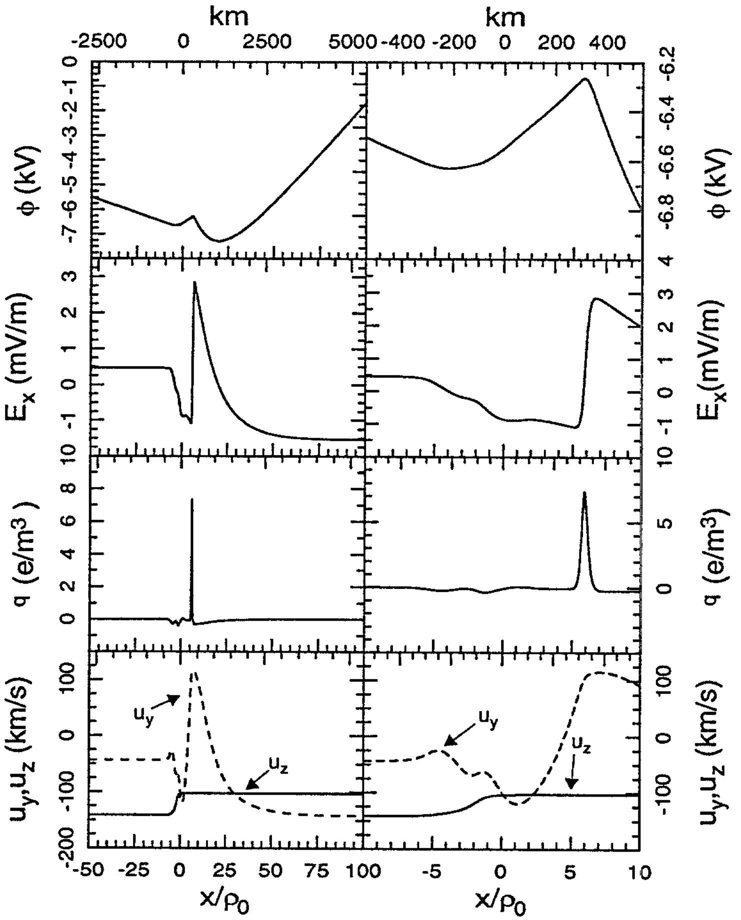

Fig. 8. Simulation of an ISEE magnetopause crossing: electric structure and bulk velocity.

neutrality condition can then be reduced to an eigenmode equation of Schrödinger's type:

$$(\mathrm{d}^2A/\mathrm{d}x^2) - (k^2 + V_0)A = 0, \tag{40}$$

where

$$V_0 = -\tfrac{4\pi}{k^2}\left[\hat{a}^2\Psi + \tfrac{1}{\alpha}\left(\hat{a}\tfrac{\partial\Psi}{\partial\phi}\right)^2\right], \quad \hat{a} = k_z\frac{\partial}{\partial a_y} - k_y\frac{\partial}{\partial a_z},$$

and

$$\Psi(a_y, a_z, \phi) = \sum_\nu n^\nu T^\nu, \quad \alpha(a_y, a_z, \phi) = e^2\sum_\nu \frac{n^\nu}{T^\nu}.$$

The solution of Equation (40), satisfying the natural boundary conditions $A(x \to \pm\infty) \to \exp(\mp kx) \to 0$, has a jump of the logarithmic derivative $R(x) = \mathrm{d}\ln A/\mathrm{d}x$ at $x = x_s$:

$$\Delta'(x_s, k) = R^+(x \to x_s + 0) - R^-(x \to x_s - 0), \tag{41}$$

which is proportional to the excess free energy that could be released by current filamentation in the vicinity of the singular surface. This term depends on the form of the equilibrium distribution functions and contains information about the global distribution of plasma and magnetic field in the layer.

For the symmetrical Harris configuration (38) the 'potential well' V_0 takes the simple form (Furth *et al.*, 1963)

$$V_0 = -2(k_z/k\mathcal{L}_H)^2 \cosh^{-2}(x/\mathcal{L}_H), \tag{42}$$

and Equation (40) can be solved analytically. The analytical expression for $\Delta'(x_s, k)$, at an arbitrary magnetic surface x_s within the symmetrical configuration (38), in terms of associated Legendre functions is presented in the paper by Kuznetsova and Zelenyi (1985). For $x_s = 0$ this expression reduces to the well-known formula $\Delta'_0 = (1 - k^2\mathcal{L}_H^2)/k\mathcal{L}_H$ (Laval *et al.*, 1966). In a general asymmetrical case, the solution of the eigenmode Equation (40) and the corresponding jump of the logarithmic derivative (41) must be obtained numerically (see Kuznetsova and Roth, 1995).

When $\Delta'(x_s, k = k_*) = 0$ the solution of the Schrödinger-type Equation (40) is smooth at $x = x_s$. The corresponding eigenvalue k_*^2 may be thought of as an 'energy level' $\mathcal{E}_k = k_*^2$ of adiabatic perturbations at $x = x_s$. For instance, at $x_s = 0$, the plane of symmetry of the Harris configuration (38), we have $\mathcal{E}_k = 1/L^2$.

When $\Delta'(x_s, k) > 0$ (for $k < k_*$) the magnetic surface x_s has an excess of free energy with respect to the excitation of the drift tearing perturbations $A_{\|}, \tilde{\varphi} \sim \exp(-i\omega t + ik_y y + ik_z z)$ with wavelength $2\pi/k$ and wave vector perpendicular to the local direction of the equilibrium magnetic field ($\mathbf{k} \cdot \mathbf{B} = 0$). Whether this tendency will be realized depends on other contributions to the energy-balance condition associated with the temporal evolution of the layer ($\partial/\partial t \sim -i\omega$) and with irreversible nonadiabatic interaction of resonant particles with perturbations in some small vicinity of the x_s plane, where $k_{\|} = (\mathbf{k} \cdot \mathbf{B}/B)$ is small and the inductive and potential parts of the parallel electric field $E_{\|} = (i\omega/c)A_{\|} - ik_{\|}\tilde{\varphi}$ cannot compensate each other.

8.1. Effect of the Relative Flow Velocity

The presence of shear flow affects the structure of the TD as well as the tearing modes (Lakhina and Schindler, 1983a, b; Zelenyi and Kuznetsova, 1984; Wang and Ashour-Abdalla, 1992). We illustrate here the modifications by the flow asymmetry to the Harris neutral sheet (configuration (38) with $|B_{y0}| \ll B_R$) separating magnetosheath and magnetospheric plasma with nearly antiparallel magnetic fields

(θ close to 180°). Kuznetsova *et al.* (1994) suggested to consider a simple equilibrium which is a combination of the models of Harris (1962) and Sestero (1966). To explore the effect of the relative flow velocity, a hydrogen plasma with the same isothermal temperature (1 keV) in each source region (Table VI) is considered and the absolute values of the asymptotic magnetic fields are assumed to be equal: B_1=B_2=B_0 = 60 nT. We choose a coordinate system in which the asymptotic plasma flow velocities, directed along the z axis, are antisymmetric, that is, $V_{1z} = +V_K$, $V_{2z} = -V_K$ ($V_K > 0$). The structure of the magnetic field is the following ($B_{y0} > 0$, $B_R > 0$, $B_{y0} \ll B_R$):

$$\begin{aligned}
&B_y(x) > 0, \quad B_z(0) = 0,\\
&B_{1y} = B_{y0}, \quad B_{2y} = B_{y0},\\
&B_{1z} = -B_R, \quad B_{2z} = +B_R,
\end{aligned}$$

Each electron/ion distribution consists of two inner (F_{i1} and F_{i2}) and two outer populations (F_1 and F_2). The distributions can be deduced from (1)–(3) by assuming:

$$\begin{aligned}
&\text{for } F_{i1} \; : N = s_0,\; \mathcal{U}_z = +V_K,\; \mathcal{U}_y = \mathcal{U}_H = -2c\mathcal{T}/ZeB_0\mathcal{L},\\
&\text{for } F_{i2} \; : N = s_0,\; \mathcal{U}_z = -V_K,\; \mathcal{U}_y = \mathcal{U}_H = -2c\mathcal{T}/ZeB_0\mathcal{L},\\
&\text{for } F_1 \;\; : N = s_1,\; \mathcal{U}_z = +V_K,\; \mathcal{U}_y = 0,\\
&\text{for } F_2 \;\; : N = s_1,\; \mathcal{U}_z = -V_K,\; \mathcal{U}_y = 0,
\end{aligned} \tag{43}$$

and by adopting the velocity distribution parameters listed in Table VI. The velocity distribution functions for both electrons and protons can then be written in the form:

$$\begin{aligned}
f = {} & \frac{1}{2}\left(\frac{m}{2\pi\mathcal{T}}\right)^{3/2} \exp\left(-\frac{2H + mV_K^2}{2\mathcal{T}}\right) \times \\
& \times \left\{ s_1 + s_0 \exp\left[-\left(\frac{\rho}{\mathcal{L}}\right)^2 - \frac{2c}{ZeB_0\mathcal{L}} p_y\right]\right\} \times \\
& \times \left\{ \operatorname{erfc}\left[-\delta_z(p_z - mV_K)\right] \exp\left(\frac{V_K p_z}{\mathcal{T}}\right) + \right. \\
& \left. + \operatorname{erfc}\left[\delta_z(p_z + mV_K)\right] \exp\left(-\frac{V_K p_z}{\mathcal{T}}\right)\right\},
\end{aligned}$$

where δ_z is given in (5) and $\mathcal{L} = \mathcal{L}_H B_R/B_0$ (Equation 34 determines the relation between $\mathcal{L}_H$ and the drift velocity of the inner particles in the y direction). The overall density distribution takes the form:

$$n = \sum_{i=1}^{2} n_i,$$

TABLE VI

Magnetopause with velocity shear

Reference parameters and boundary conditions									
	$\mathcal{T}_0$ eV	B_0 nT	k_1 k_2	ψ_2 V	x_0^*	B_1 nT	θ_0 °	a_{0y}^*	a_{0z}^*
protons	1000	60	2 4	0	0	60	−90	0	0

Plasma populations									
	N cm^{-3}	$\mathcal{T}$ eV	$\mathcal{U}_y$ km s^{-1}	$\mathcal{U}_z$ km s^{-1}	C_i	$\mathcal{L}/\rho_0$	L_z	p_{0y}^*	p_{0z}^*
Outer left populations									
Electrons	0.01	1000	0	292	1 1 0 0	–	1.5	–	0
Protons	0.01	1000	0	292	1 1 0 0	–	1.5	–	0
Inner populations									
Electrons	2.00	1000	146	292	1 1 0 0	3	1.5	–	0
Protons	2.00	1000	−146	292	1 1 0 0	3	1.5	–	0
Electrons	2.00	1000	146	−292	0 0 1 1	3	1.5	–	0
Protons	2.00	1000	−146	−292	0 0 1 1	3	1.5	–	0
Outer right populations									
Electrons	0.01	1000	0	−292	0 0 1 1	–	1.5	–	0
Protons	0.01	1000	0	−292	0 0 1 1	–	1.5	–	0

with

$$n_i = \frac{1}{2}\left[s_1 + s_0 \exp\left(-\frac{2a_y}{B_0\mathcal{L}}\right)\right] \times$$
$$\times \exp\left\{-\frac{Ze}{\mathcal{T}}\left[\phi + \frac{(-1)^i V_K a_z}{c}\right]\right\} \operatorname{erfc}\left[(-1)^i \frac{a_z}{B_0 L_z \rho_0}\right],$$

a result that is obtained using the moments calculated in Appendix A.

The structure of the configuration is only determined by the flow asymmetry factor $\zeta = V_K/|\mathcal{U}_H^+|$, where $\mathcal{U}_H^+$ is the drift velocity of the inner ions (Equation (43)). Assuming $a_y(0) = a_z(0) = 0$, it is clear from the quasi-neutrality condition that $\phi(0) = 0$. From (21) and (28) (where $\psi_2 = 0$), it can be seen that the parameter s_1 is equal to the symmetrical asymptotic number densities ($s_1 = 0.01$ cm^{-3}). Because of the symmetry of the transition with respect to $x = 0$, and from (19), (24), and (13), the asymptotic electric potentials should be identical:

$\phi(x \to \pm\infty) = (V_K/c)B_{y0}|x| +$ constant. The parameter s_0 characterizes the number density at the center of the layer: $n(x = 0) = s_0 + s_1$. The asymptotic number density s_1 is chosen very small in comparison with the density inside the MCL (in order to compare with the Harris model), that is, $s_1 \ll s_0$. The value of the input parameter s_0 is determined by the asymmetry factor ζ in the following way: for a fixed value of ζ, an iterative method is used to find the value of s_0 corresponding to $\theta \approx 170°$ ($B_{y0} = 0.08\ B_R$), that is, to nearly opposite directions of the asymptotic magnetic fields. The values of V_K and $|\mathcal{U}_H^+|$ correspond to $\zeta = 2$. For that value of ζ, it is found that $s_0 = 2\ \mathrm{cm}^{-3}$ is the number density of inner particles required for a magnetic field rotation $\theta = 173.6°$. The configuration reduces to the Harris plane neutral sheet (with b=$0.08B_R$) when ζ tends to zero.

Figure 9 illustrates the structure of the MCL for $\zeta = 2$. Figure 9 shows that the relative flow velocity results in the generation of a strong B_y component in the center of the layer ($B_y(0) \gg B_{y0}$). For $\zeta = 2$, $B_y(0)$ becomes comparable to B_R. Therefore, in the presence of a shear flow in the MCL with $\theta \to 180°$, the magnetic field is expected to rotate from one direction to another, rather than to change its sign only. For negative V_K the bulk flow velocity has a nonrealistic oscillating profile inside the current layer. However, simultaneous change of the sign of B_{y0} and V_K (which is equivalent to change of the coordinate system, $y \to -y$, $z \to -z$) corresponds to configurations similar to those shown in Figure 9. Therefore, for $\theta \to 180°$, the sense of magnetic field rotation is likely to be related to the direction of the flow in the magnetosheath: it should be opposite in the northern and southern hemispheres. Experimental data, discussed by Sonnerup and Cahill (1968) and Su and Sonnerup (1968), appear to be consistent with this prediction. A number of dayside magnetopause flow reversal events observed by ISEE-2 have been reported by Gosling *et al.* (1990). A preliminary analysis seems to indicate that, in those cases where also a large magnetic shear is present, the sense of magnetic field rotation is related to the direction of the magnetosheath flow: it is clockwise in the northern dayside hemisphere, and anti-clockwise in the southern dayside hemisphere. Also, in heliospheric current sheet crossings observed by the WIND spacecraft, the magnetic field had almost antiparallel directions on both sides and did rotate with nearly unchanged magnitude rather than change its sign only (Szabo *et al.*, 1995). These recent observations are consistent with the important role attributed to the velocity shear.

The dependence of $B_y(0)/B_0$ on the relative flow velocity is shown on Figure 10 for different values of the layer thickness, while keeping the value of $\theta \approx 170°$. In Figure 10 the shear flow velocity $2V_K$ is normalized to $2v_0$, that is, $V_K/v_0 = \zeta\rho_0/\mathcal{L}$, while the thickness is measured in ion Larmor radius and expressed in terms of the parameter $\mathcal{L}_H$ of the Harris model by using the relation $\mathcal{L}_H/\rho_0 \approx \mathcal{L}/\rho_0$ (valid for the case where the asymptotic fields are nearly antiparallel). It can be seen that decreasing/increasing the value of the relative flow velocity can lead to the same intensity of $B_y(0)/B_0$, provided the thickness is increased/decreased. On the other hand, the factor of asymmetry, $\zeta = V_K/|\mathcal{U}_H^+| = (V_K/v_0)(\mathcal{L}/\rho_0)$, is

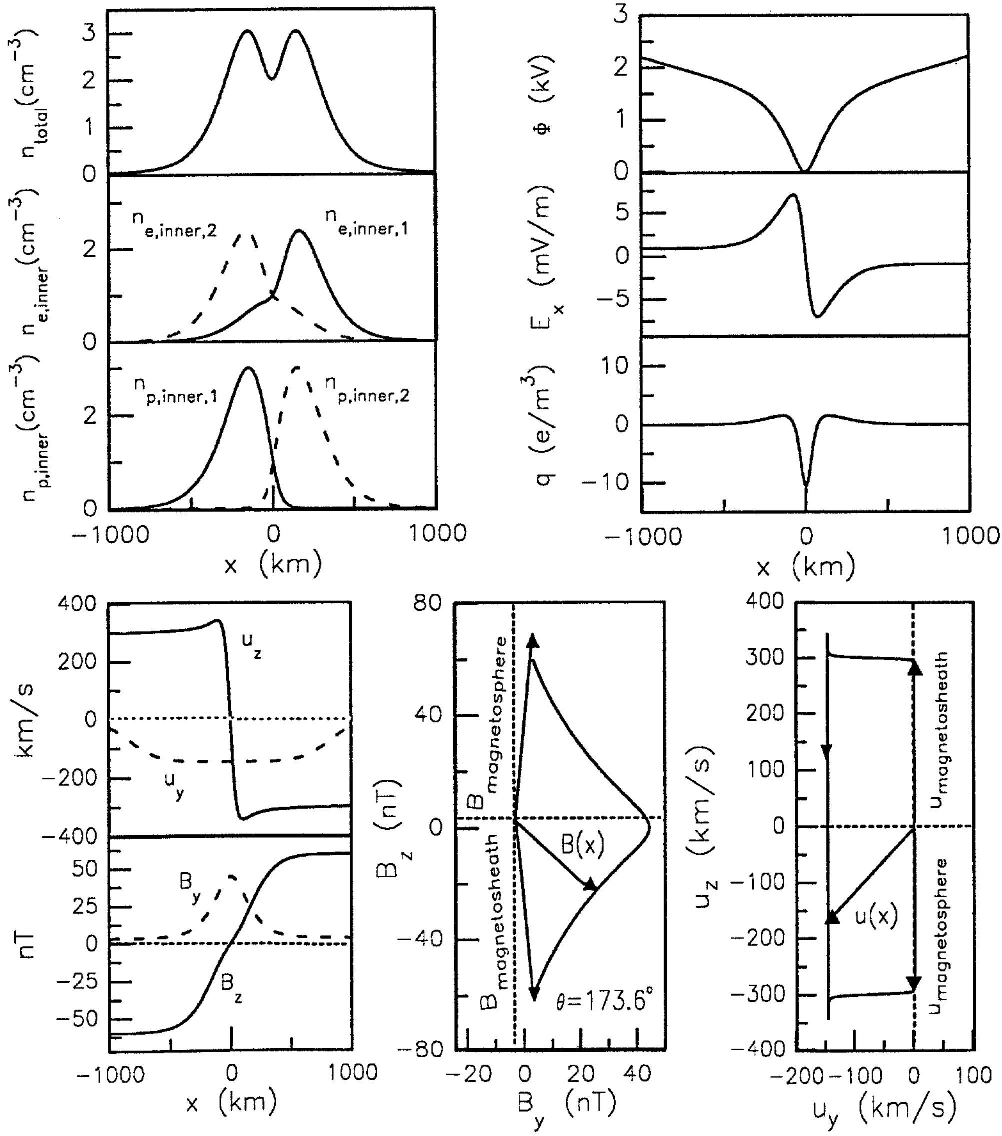

Fig. 9. Magnetopause with velocity shear: physical structure.

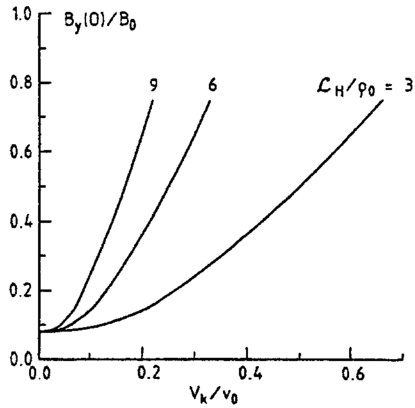

Fig. 10. Dependence of the B_y component of the magnetic field at $x = 0$ (normalized on B_0) on the shear flow V_K (normalized on v_0) for different values of the MCL thickness, while keeping the value of $\theta \approx 170°$. In this figure the thickness is measured in ion Larmor radii and is expressed in terms of the parameter $\mathcal{L}_H$ of the Harris model by using the relation $\mathcal{L}_H \approx \mathcal{L}$ valid for the case where the asymptotic fields are nearly antiparallel. It can be seen that decreasing the value of the shear flow can lead to the same intensity of the B_y component at $x = 0$, provided the thickness is increased.

directly proportional to $\mathcal{L}$. Clearly, for a fixed value of V_K/v_0 this factor increases proportionally to the thickness of the layer ($\mathcal{L}_H/\rho_0$), because of a decrease of the ion drift velocity ($|\mathcal{U}_H^+|$). This results in a decrease of s_0 and, consequently, from the pressure balance condition, to an increase of $B_y(x = 0)/B_0$, as illustrated in Figure 10. This increase of $B_y(0)/B_0$ with $\mathcal{L}_H$, for a fixed V_K, can be explained by the new distribution of the current density, resulting from the larger value of the thickness, which modifies the integrated z component of the current density $\int_{-\infty}^{0} J_z \, dx$, responsible for the generation of $B_y(0)$. This integrated component, which is proportional to $V_K\mathcal{L}_H$, is indeed increasing with the growth of $\mathcal{L}_H$ for a fixed V_K, while the integrated y component $\int_{-\infty}^{+\infty} J_y \, dx \sim |\mathcal{U}_H^+|\mathcal{L}_H$, supporting the initial (Harris) inversion of the magnetic field or the total variation of B_z ($\approx 2B_0$) is independent of $\mathcal{L}_H$. Thus the thicker the Harris layer given by configuration (38) (with $B_{y0} \ll B_0$), the easier 'to spoil' it by smaller values of the relative flow velocity.

The flow asymmetry modifies the potential well (42) corresponding to the symmetrical Harris case ($\zeta = 0$), in the following way:

$$V_0 = \frac{B_z{}'}{B_z} + \frac{B_y B_y{}'}{B_z B_0 \mathcal{L}_H}.$$

The free energy of perturbations is illustrated in Figure 11 for the central magnetic surface $x = 0$. It is seen that the curves 'ζ=0' (Harris case) and '$\zeta = 2$' are close to each other only in the narrow interval of wavelength: $0.5 < k\mathcal{L}_H < 0.8$.

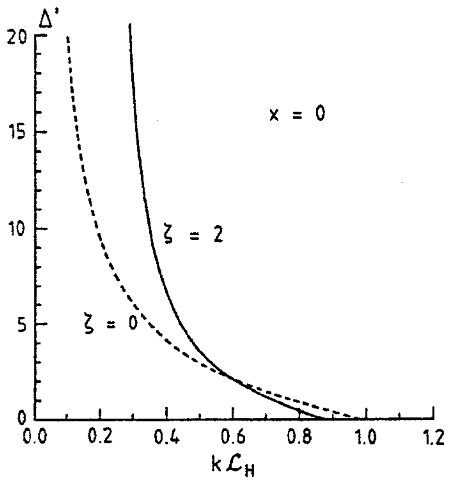

Fig. 11. The dependence of the free energy of perturbations Δ' of the central magnetic surface $x = 0$ on the wave number $k\mathcal{L}_H$. The solid curve corresponds to a finite value of the flow asymmetry factor ($\zeta = 2$). For comparison, the corresponding profile of Δ' for the symmetrical Harris configuration ($\zeta = 0$) is illustrated by the dashed curve.

For longwave perturbations, $k\mathcal{L}_H < 0.5$, the free energy is strongly modified. Specifically, for $0 \ll k\mathcal{L}_H = m^*$,

$$[\Delta'(k\mathcal{L}_H = m^*, \zeta)]^{-1} = 0.$$

For $k\mathcal{L}_H \rightarrow m^*$ the perturbed vector potential and, consequently, also the normal perturbation of the magnetic field tend to zero near the singular surface $x = 0$. The $x = 0$ singular surface itself remains unperturbed; meanwhile the peripheral magnetic surfaces experience the rippling-type distortions instead of reconnection. Thus with the increase of the wavelength, the quasi-symmetrical tearing mode transforms into the asymmetrical kink mode. For $k\mathcal{L}_H < m^*$ the free energy changes sign, and the mode of 'negative energy' transforms therefore to the mode of 'positive energy'. Such transformation of the mode type in the longwave limit ($k\mathcal{L}_H < m^* = x/\mathcal{L}_H$) for perturbations of the peripheral magnetic surfaces ($x/\mathcal{L}_H \neq 0$) in the symmetrical Harris configuration was considered in detail in Kuznetsova and Zelenyi (1985).

Assuming that for shortwave perturbations ($m^* \ll k\mathcal{L}_H < 0.8$), $\Delta'(\zeta) \approx \Delta'_0$, it is easy to compare the growth rate of the tearing mode $\gamma(\zeta)$, modified by the shear flow, with the well-known expression for the growth rate of the electron tearing mode (γ_e), excited in the center of the symmetrical Harris configuration

$$\frac{\gamma(\zeta)}{\gamma_e} = \frac{n_0}{n(0)} \frac{B_{y0}}{B_y(0)} \frac{B'_z(0)\mathcal{L}_H}{B_R}, \tag{44}$$

where $n_0 = n(0)$ for $\zeta = 0$, $B_{y0} = B_y(x \rightarrow \mp\infty) \ll |B_z(x \rightarrow \mp\infty)| = B_R$. For $\theta \approx 170°$ and $V_K > |\mathcal{U}_H^+|$ the ratio $B_{y0}/B_y(0)$ could be very small. It is seen from Equation (44) that the growth of the tearing instability will be significantly suppressed by the large value of the magnetic field $B_y(0)$ generated by the shear flow at the center of the current layer.

8.2. Effect of Magnetic Field Asymmetry

The MCL simulation described by Table VII is taken from Kuznetsova and Roth (1995). The magnetosheath corresponds to $x = -\infty$, while the magnetosphere is at $x = +\infty$. There is no velocity shear. The reference particle is a 1000 eV proton in a magnetic field of 40 nT; this corresponds to the magnetosheath ions. From Equations (B.2) and (29), one finds $\rho_0 \approx 115$ km, while $\psi_2 = 3.8$ statvolts = 1142 V. There are 3 distinct plasmas: the magnetosheath plasma, an inner plasma and the magnetospheric plasma, each of which consists of one proton and one electron component. All electron populations have the same thermal energy; the same is true for all protons. The integration starts from the center of the transition ($x_0^* = 0$) where the magnetic field is inclined by $-90°$ with respect to the z axis. The values of $B_y(0)$ and $\phi(0)$ are obtained from the pressure balance condition and from the quasi-neutrality equation.

This example has been constructed in such a way that the outer electrons as a whole ($\nu_1 = 1$ and $\nu_2 = 1$) are characterized by an isotropic Maxwellian distribution. Indeed, the values of $\mathcal{N}$, C_k, and $N^{j_2=1}$ in Table VII are chosen such that:

$$F^-_{\text{outer}} = F^{\nu_1=1} + F^{\nu_2=1} = N^- \left(\frac{m^-}{2\pi\mathcal{T}^-}\right)^{3/2} \exp\left(-\frac{H^-}{\mathcal{T}^-}\right),$$

where, from Equation (21), $N^- = n(-\infty)$. For the inner particles, the partial velocities (u_y, u_z) and temperatures (T_x, T_y, T_z, and T) do not vary across the transition layer, that is, $u_y = \mathcal{U}_y$, $u_z = 0$, $T_x = T_y = T_z = T = \mathcal{T}$. In particular, the temperature of the inner electrons does not vary. The total electron temperature also does not vary across the transition, since the outer electrons are isotropic. The current along the y-axis is carried only by the inner particles (for which $u_z = 0$). As $u_y = 0$ for the outer populations, these carry the current along the z-axis. This can also be inferred from their distributions, as $G(U_y, U_z)$ in (3) reduces to $\frac{1}{2}$ erfc$(-U_z)$ for the particles originating from $x = -\infty$, and to $\frac{1}{2}$ erfc$(+U_z)$ for the particles originating from $x = +\infty$, because of the particular choice of the C_k. This explains the lack of p_y dependence in the velocity distribution of the outer populations, so these particles do not flow in the y direction.

The values of $\mathcal{U}_y$ for the inner particles have been computed from (34), with $B_R = |B_{1z}|$; $\mathcal{L}_H = \mathcal{L}B_1/|B_{1z}|$; $\mathcal{L} = 4\rho_0 \approx 460$ km. The values of N for the inner populations control the angle of magnetic field rotation θ, because they determine the current along y, which is responsible for the reversal of the B_z component. In this example B_1, B_2, and $\mathcal{N}^{\nu_2}$ are fixed. $\mathcal{N}^{\nu_1}$ can then be derived from the pressure balance condition. In Kuznetsova and Roth (1995) an iterative method is employed

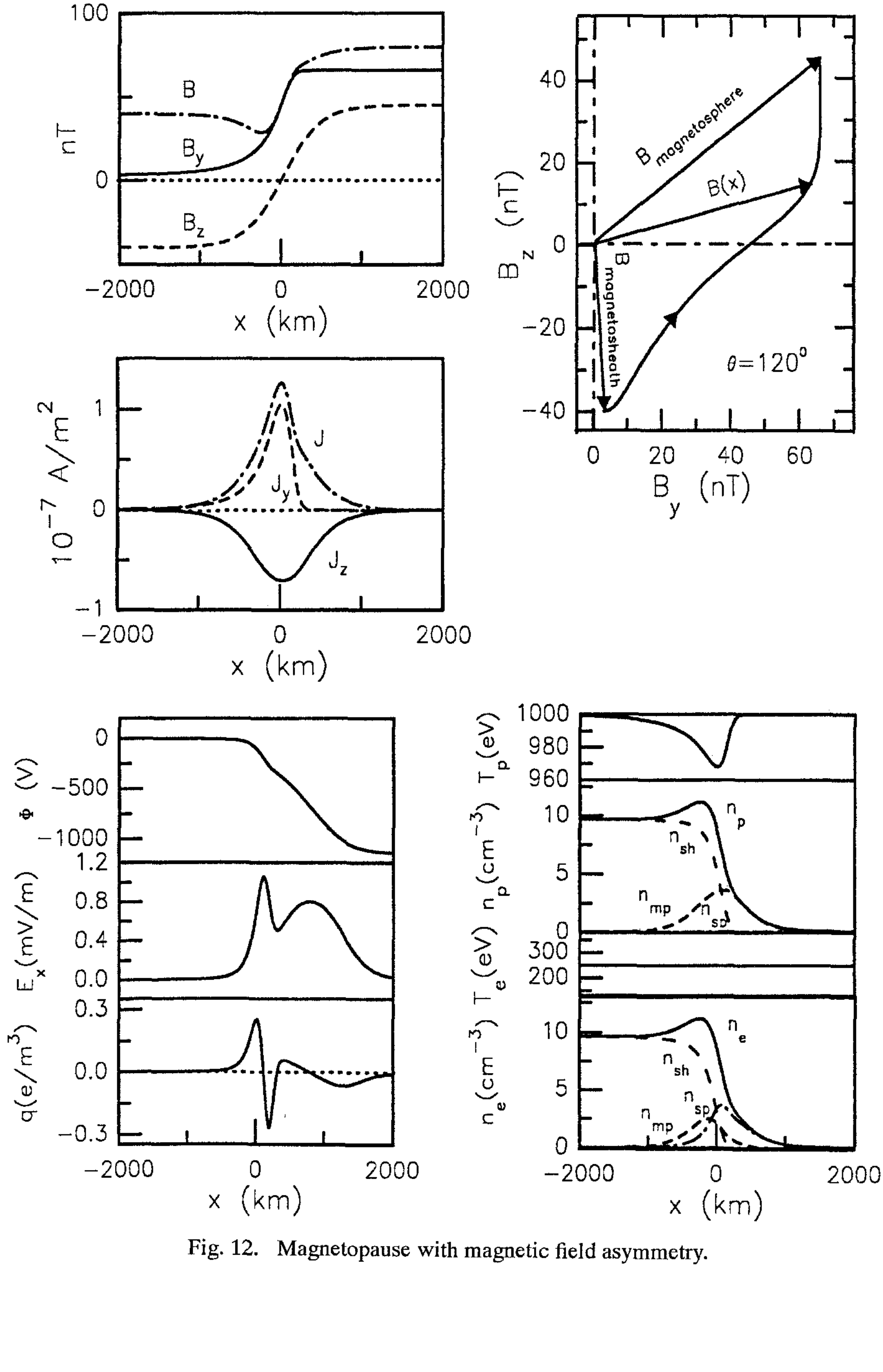

Fig. 12. Magnetopause with magnetic field asymmetry.

TABLE VII

Magnetopause with magnetic field asymmetry

Reference parameters and boundary conditions									
	$\mathcal{T}_0$ eV	B_0 nT	k_1 k_2	j_2 N^{j_2} cm^{-3}	x_0^*	B_1 nT	θ_0 °	a_{0y}^*	a_{0z}^*
Protons	1000	40	2 4	1 9.65	0	40	-90	0	0

Plasma populations									
	N cm^{-3}	$\mathcal{T}$ eV	$\mathcal{U}_y$ km s^{-1}	$\mathcal{U}_z$ km s^{-1}	C_i	$\mathcal{L}/\rho_0$	L_z	p_{0y}^*	p_{0z}^*
Outer left populations									
Electrons	9.65	250	0	0	1 1 0 0	–	2	–	0
Protons	9.65	1000	0	0	1 1 0 0	–	2	–	0
Inner populations									
Electrons	3.16	250	27.4	0	1 1 1 1	4	–	–	–
Protons	3.16	1000	−109.4	0	1 1 1 1	4	–	–	–
Outer right populations									
Electrons	0.10	250	0	0	0 0 1 1	–	2	–	0
Protons	0.10	1000	0	0	0 0 1 1	–	2	–	0

to find the value of $N_i = N^{\nu_i=1} = N^{\nu_i=2}$ corresponding to θ = 120°. Figure 12 shows the magnetopause structure; the hodogram illustrates that the magnetic field rotation $\theta \approx 120°$.

Two groups of Vlasov equilibria were illustrated in Kuznetsova and Roth (1995). The first group (referred to as case I) corresponds to situations where an increase of the thermal pressure in the magnetosheath (B_1 = 40 nT is fixed) causes an earthward displacement of the MCL (B_2 is increasing, $\mathcal{N}^{\nu_2} = 0.1$ cm^{-3} is fixed). Magnetic field hodograms and number density profiles for fixed B_1 =40 nT and different values of B_2 and θ are shown in the left columns of Figures 13 and 14. The second group (referred to as case II) corresponds to situations where the positions of the MCL are fixed (B_2 = 80 nT and $\mathcal{N}^{\nu_2} = 0.1$ cm^{-3} are fixed), while any increase of the thermal pressure in the adjacent magnetosheath results in a corresponding reduction of the magnetic pressure (B_1 is decreasing). Magnetic field hodograms and number density profiles for fixed B_2 = 80 nT and different values of B_1 and θ are shown in the right columns of Figures 13 and 14. The number density profiles in Figure 14 are illustrated as a function of the distance x/ρ_0 from the center of the layer $x = 0$, where $\rho_0 = \lambda_{\mathcal{L}} = c(2\mathcal{T}_0 m^+)^{1/2}/eB_0$ is

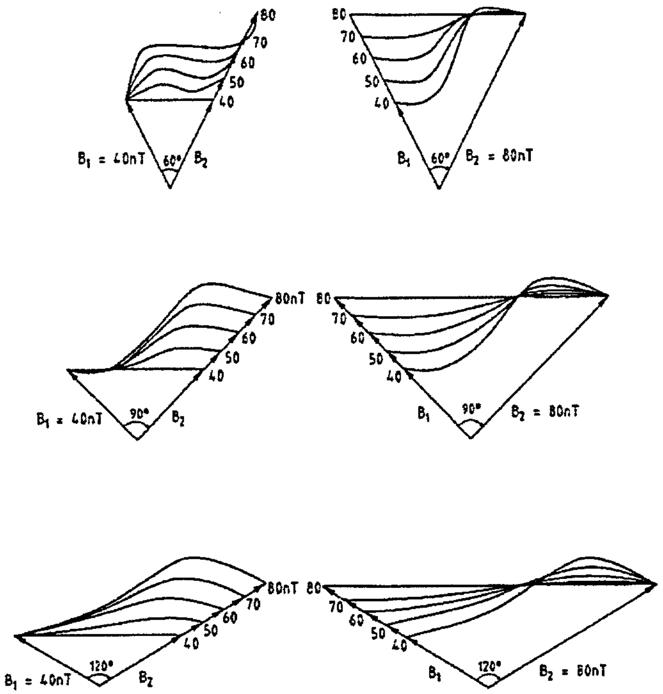

Fig. 13. Hodograms of **B** in the MCL for different values of B_1, B_2, and θ.

a typical ion Larmor radius ($\mathcal{T}_0 = 1$ keV, $B_0 = 40$ nT). Table VII remains nearly identical for all simulations in both groups. Only the values of B_1, $\mathcal{U}_y$ for the inner particles, $\mathcal{N}^{\nu_1} = N^{j_2}$ (determined from the pressure balance condition), and N_i (determined by an iterative method as a function of θ) may differ from one simulation to another.

In both groups, the internal structure of the MCL depends on two parameters characterizing the magnetic field asymmetry: the asymmetry factor $\kappa_B = (B_2 - B_1)/B_2$ and the angle of the magnetic field rotation θ. These parameters determine in particular the plasma density and the magnetic field at the center of the layer. When the asymmetry factor κ_B tends to zero the configuration reduces to the symmetrical modified Harris model (38) with a rarefied background. The peak in density in the center of the layer is associated with the inner populations (the relative contribution of which to the total number density increases with increasing angle θ) and is likely to be a general feature of a current sheet with large magnetic shear. It is seen that the introduction of asymmetry in case I (the left column) significantly modifies the number density in the center of the layer, while in case II (the right column) the number densities at $x = 0$ are only slightly different for various asymmetry factors.

One-dimensional current layers with magnetic shear are thermodynamical non-equilibrium systems that have an excess of free energy and are potentially unstable

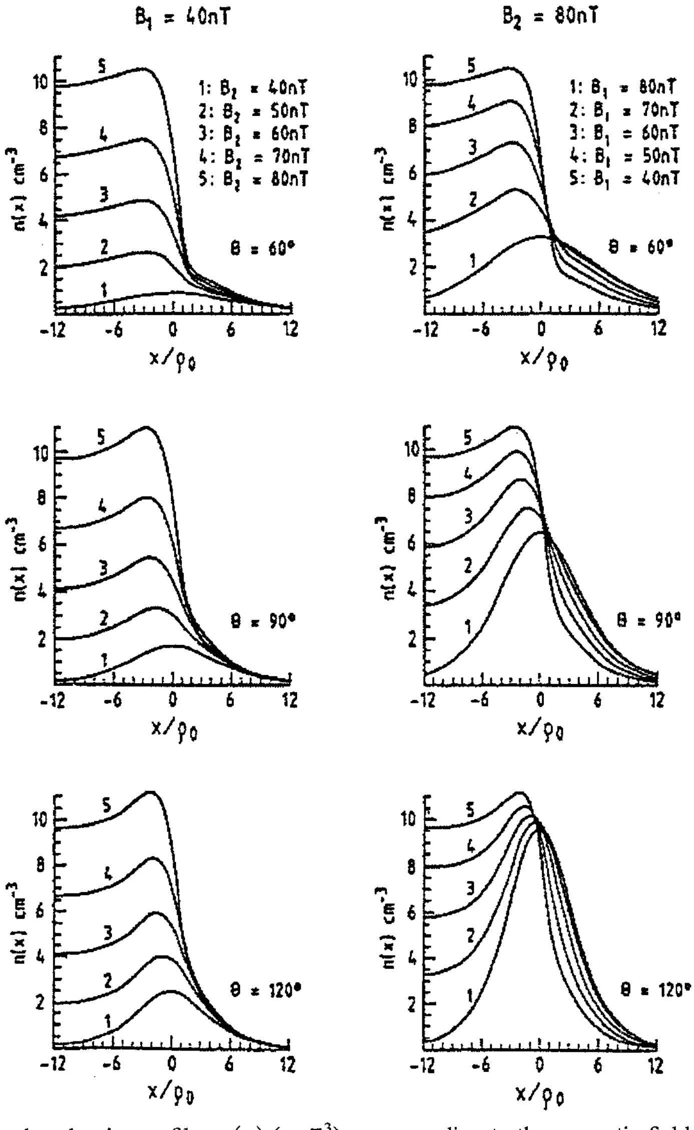

Fig. 14. Number density profiles $n(x)$ (cm^{-3}) corresponding to the magnetic field hodograms of Figure 13.

with respect to the excitation of large scale, electromagnetic perturbations, resulting in the destruction of magnetic surfaces. In Kuznetsova and Roth (1995) and Kuznetsova *et al.* (1995) the free energy and the 'energy level' of adiabatic perturbations (with wave vectors **k**) were evaluated. The stochastic percolation model suggested by Galeev *et al.* (1986) (hereafter referred to as the GKZ model), based on the symmetrical charge-neutral modified Harris equilibrium, was generalized in Kuznetsova and Roth (1995), for the sets of equilibria illustrated in Figures 13 and 14. In the GKZ model, reconnection was considered as an irregular multiscale process associated with the magnetic field diffusion caused by the self-consistently generated magnetic turbulence. If the distance between the singular magnetic surfaces (where $\mathbf{k} \cdot \mathbf{B}=0$) corresponding to unstable modes is less than the ion Larmor radius, the overlap of magnetic islands growing on neighboring magnetic surfaces results in stochastic wandering of magnetic field lines from one magnetic surface to another (Rosenbluth *et al.*, 1966). This stochastic process leads to the formation of percolated magnetic filaments which connect the two sides of the current layer via an irregular path (Galeev *et al.*, 1986, Figure 1(a)). If regions of stable magnetic surfaces wider than the ion gyroradius exist within the MCL, the stochastic wandering of magnetic field lines does not result in percolation, i.e., the topological connection of magnetosheath and magnetospheric field lines is absent (Galeev *et al.*, 1986, Figure 1(b)). Therefore the necessary condition for magnetic percolation through the MCL appears to be the destruction of all magnetic surfaces within it. This condition imposes a bound on the thickness of the MCL, required for the formation of reconnection 'patches' with characteristic spatial scales along the magnetopause $\lambda_z \times \lambda_y \sim \lambda_{\text{ext}}^2$.

The energy balance equation for the tearing mode development can be represented in the following form

$$\Delta' = U_e + U_i. \tag{45}$$

The right-hand side of Equation (45) is a total non-adiabatic response which is proportional to the perturbed electric field work upon the singular current ($J_{\|} = \sigma_{\|} E_{\|}$). The values of these terms are controlled by the local values of the magnetic field and electron density in the vicinity of the singular surface $x = x_s$. The term U_e describes the irreversible increase of resonant electron energy. The term U_i is the energy expenditure for the excitation of field-aligned ion oscillations, which carry the wave energy away from the interaction region (where $k_{\|} \approx 0$) and slow down the growth of the electron drift tearing mode. At the stability threshold, the energy of ion-sound oscillations is exactly equal to the free energy of the instability: $U_i = \Delta'$.

The integral expressions for nonadiabatic contributions U_e and U_i for the general case and the numerical solution of the marginal condition $\Delta' = U_i$ for the sets of equilibria illustrated in Figures 13 and 14 are presented in the paper by Kuznetsova and Roth (1995). It is shown that the 'most unstable' magnetic surfaces (with the widest wavelength range of unstable modes) are located close to the maxima of

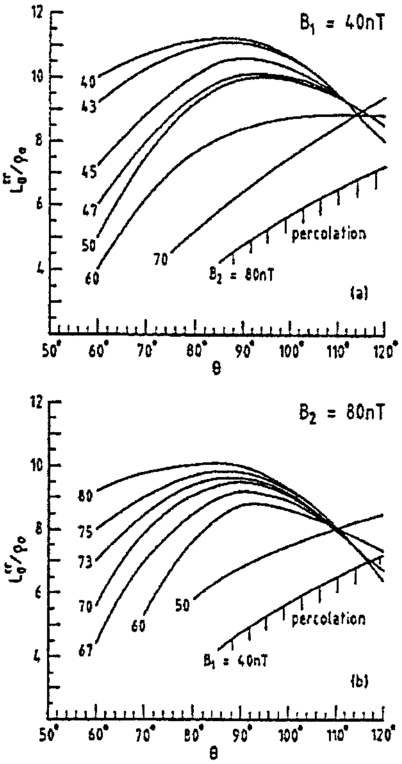

Fig. 15. Dimensionless marginal magnetopause thickness L_0^{cr}/ρ_0, for typical spatial scale of the reconnection patch $\lambda_{\rm ext} = 90\rho_0 \approx 10\,000$ km, as a function of θ for different values of B_1 and B_2. Here $\rho_0 = c(2\mathcal{T}_0 m^+)^{1/2}/eB_0 \sim 115$ km is a typical ion Larmor radius ($\mathcal{T}_0 = 1$ keV, $B_0 = 40$ nT). (a) case I ($B_1 = 40$ nT and $\mathcal{N}_2 = 0.1$ cm^{-3} are fixed, B_2 is increasing from 40 nT to 80 nT); (b) case II ($B_2 = 80$ nT and $\mathcal{N}_2 = 0.1$ cm^{-3} are fixed, B_1 is decreasing from 80 nT to 40 nT).

the number density profiles where the stabilizing influence of the coupling with ion field-aligned oscillations appears to be inefficient. On the contrary, the 'most stable' magnetic surfaces (where the marginal wavelength for the instability is maximal) are located in regions with the strongest density gradients, where drift effects are the most prominent and where perturbations are strongly coupled with ion sound oscillations.

One can assume that the characteristic spatial scale along the magnetopause, $\lambda_{\rm ext}$, is determined by external conditions (the size of the magnetopause, the convection pattern in the magnetosheath). The dependence of the marginal magnetopause thickness L_0^{cr}/ρ_0 on θ for $\lambda_{\rm ext} = 90\rho_0 \approx 10\,000$ km and different κ_B is shown in Figure 15. A MCL of thickness less than the marginal one (L_0^{cr}) will be subject to percolation of magnetic field lines. The results shown on Figure 15 represent the generalization of the GKZ model to the asymmetrical case. Note that for the symmetrical case ($\kappa_B = 0$, $B_1 = B_2$) the characteristic thickness L_0^{cr} is linked to the characteristic thickness L_0^{GKZ} used in the GKZ model ($L_0^{\mathrm{GKZ}} = 2\mathcal{L}_H$) by the relation $L_0^{cr}/L_0^{\mathrm{GKZ}} = \sin(\theta/2)$.

In the GKZ model, northward orientation of the IMF was found to be optimum for the percolation, that is, the maximum thickness of Harris-type layers subjected to percolation is achieved for $\theta < 90°$. The introduction of asymmetry $\kappa_B \neq 0$ in the magnetic field helps to overcome this seeming contradiction with experimental data (Berchem and Russell, 1984; Southwood *et al.*, 1986). When $\theta < 90°$, it can be seen that even for small values of the asymmetry factor ($\kappa_B \geq 0.15$) the marginal thickness L_0^{cr} is significantly decreased, that is, only thin MCLs can be subject to percolation. Therefore the most favorable angle for percolation (θ^*) is shifted to larger values: $\theta^* > 90°$ (southward IMF). The larger the asymmetry factor κ_B, the larger the angle θ^*. For very asymmetrical MCLs ($\kappa_B \geq 0.4$), $\theta^* \geq 120°$. It is reasonable to assume that the curves shown in Figure 15 qualitatively reflect the dependence of the characteristic magnetopause thickness (normalized on a typical ion Larmor radius $\rho_0 = c(2\mathcal{T}_0 m^+)^{1/2}/eB_0 \sim 115$ km for $\mathcal{T}_0 = 1$ keV, $B_0 = 40$ nT) on the angle θ and the plasma beta in the magnetosheath (which for $\mathcal{N}_2 \approx 0$ can be expressed through the asymmetry factor κ_B: $\beta = \kappa_B(2 - \kappa_B)/(1 - \kappa_B)^2$). One can see that in realistic asymmetrical cases ($\kappa_B > 0.3$) the magnetopause should be thinner for $\theta < 90°$ (northward IMF) than for $\theta > 90°$ (southward IMF). For southward IMF ($\theta > 90°$) the magnetopause thickness depends only slightly on κ_B and β. For northward IMF the magnetopause should be thinner for larger values of β in the magnetosheath.

9. Formation of Discrete Auroral Arcs

In this section we model the electrical structure of a sheath which separates magnetosperic particle populations of different densities and temperatures (Roth *et al.*, 1993). With plasma parameters typical of the Earth's outer magnetoshere and plasmasheet, we obtain results bearing many features pertinent to magnetospheric processes, specifically the origin of discrete auroral arcs. Although we do not know precisely where the various particle features in the geomagnetic tail map to in the ionosphere (Parks *et al.*, 1992), the present computed transition can equally be representative of the plasmasheet boundary layer (PSBL) in the tail that, following Eastman *et al.* (1984), maps to discrete auroral arcs, or to the boundary of some plasmasheet 'cloud' immersed in the central plasmasheet (CPS): another location which has also been suggested for the mapping of discrete arcs (e.g., Elphinstone *et al.*, 1991; Zelenyi *et al.*, 1990). In this section, we therefore loosely refer to the high altitude plasma transitions where aurorae map as being 'magnetospheric plasma boundary layers' between plasmasheet 'clouds' and their magnetotail 'background'.

9.1. The Auroral Circuit

The magnetospheric D.C. generator, or EMF, which sustains the dissipative current in the auroral circuit, should be identified with the potential differences generated across these magnetospheric plasma boundary layers (in this context D.C. means that these potentials and associated currents do not oscillate and reverse sign but is not to mean that the situation is totally time stationary). The analog of this magnetospheric D.C. generator is the contact potential difference produced at the interface between two metallic conductors at different temperatures. There are also other devices and physical mechanisms capable of producing large potential differences and electric current systems; e.g., the dynamo effect arising from the relative motion of conductors or plasma clouds in the presence of a magnetic field. In the case of dynamo action in the magnetosphere, the electric field is generally called the convection electric field and extends over the whole volume of moving plasma. For plasma velocities of less than 100 km s^{-1} in the presence of magnetic fields of 40 nT or less, this convection electric field ($\mathbf{E} = -\mathbf{V} \times \mathbf{B}$) does not exceed 4 mV m^{-1}. However, because the scale size of plasma motions can be very large, the total potential difference involved may be in excess of 100 kV in the case of the solar wind's motion with respect to the Earth. In contrast, the charge separation thermoelectric field strengths treated in this section can have much larger values (100–200 mV m^{-1}) although such fields are confined to very thin layers at the edges of plasma irregularities.

When modeling the EMF, we use a TD model. Therefore the currents in the boundary are perpendicular to the charge separation electric field. In effect, this is an 'unloaded' source of EMF and no energy dissipating currents are flowing. The actual acceleration and precipitation of electrons that creates an auroral arc requires that a current system be established that threads both the source of EMF and the ionosphere by means of magnetic field-aligned currents. Figure 16 illustrates the plasma discontinuity generating an EMF at the surface of a plasma sheet density irregularity, and its projection in the terrestrial ionosphere. We expect that the presence of turbulent wave fields will scatter electrons into the atmospheric loss cone so that they will be accelerated and precipitated to produce aurorae. Moreover, the same wave fields will pitch-angle scatter charged particles that originate from the ionosphere out of their source cone so that a current system threading both the EMF and the ionosphere by means of field-aligned currents will be established.

9.2. A Magnetospheric D.C. Generator

Although the plasmasheet is rarely in a stationary state, we assume that the structure of the EMF source does not change significantly over the characteristic period of time required for an Alfvén wave to traverse it. We also consider that the radius of curvature of the boundary layer is much larger than its characteristic thickness, which is of the order of a few ion gyroradii. Under these circumstances the plasma

TABLE VIII

A magnetospheric generator

Reference parameters and boundary conditions										
	T_0 eV	B_0 nT	k_1 k_2	ψ_2 V	x_0^*	B_1 nT	θ_0 °	a_{0y}^*	a_{0z}^*
Protons	12000	40	1 2	−3500 −1650 0 +3500	0	40	0	0	0

Plasma populations									
	N cm^{-3}	T eV	$\mathcal{U}_y$ km s^{-1}	$\mathcal{U}_z$ km s^{-1}	C_i	L_y	L_z	p_{0y}^*	p_{0z}^*
Outer left populations									
Electrons	0.50	2500	0	0	1 0 1 0	0.011	–	0	–
Protons	0.50	12000	0	0	1 0 1 0	1	–	0	–
Outer right populations									
Electrons	0.15	800	0	0	0 1 0 1	0.006	–	0	–
Protons	0.15	3000	0	0	0 1 0 1	0.5	–	0	–

layer can be considered as planar. Furthermore, since in general the magnetic field direction does not vary by more than 10° or 20° from one side of a transition layer to the other side, we can consider that the direction of **B** does not change nor reverse across the transition layer although the scalar magnitude of **B** may vary. We assume, therefore, that the magnetic field direction is everywhere parallel to the z axis. By applying the Vlasov kinetic theory of the 1-D transition layer used in this review, we are actually modeling the electric field structure for an 'unloaded' source of EMF . However, to at least zero order, a description of the electric field structure for the case of an unloaded EMF will also represent the loaded case quite well. Indeed, the available potentials and field intensities will change only slightly in going from a situation of no load to a loaded situation where there is a component of the total current that is flowing parallel to **E** (so that $\mathbf{E} \cdot \mathbf{J} \neq 0$).

The plasma boundary conditions in Table VIII describe a plasmasheet cloud ($x \to -\infty$) and the background magnetotail plasma ($x \to +\infty$). There are no inner populations. The parameters L_y and L_z correspond to $l_y = l_z = 1$, i.e., to velocity distributions of Sestero type describing the sharpest transition. The plasma temperatures and densities, and the magnetic field strength are typical conditions found in the Earth's outer magnetosphere and plasmasheet. Actually, we derived

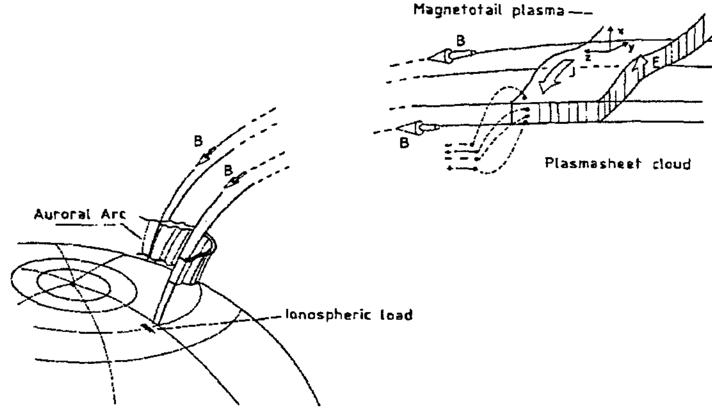

Fig. 16. Illustration of a plasma discontinuity generating an EMF at the surface of a plasmasheet density irregularity (cloud or plasmasheet-lobe boundary), and its projection in the terrestrial ionosphere. Electric potential differences are produced by thermoelectric charge separation at the interface between the two plasma regions and are distributed transverse to the magnetic field in the x-direction. These potential differences map down into the ionosphere and drive Pedersen currents, provided the local ionospheric conductivity is large enough. Due to micro-instabilities in the interface region, electrons are scattered in the loss cone; they enhance the ionization at low altitude and increase the Pedersen conductivity. Large Pedersen currents flow in the ionosphere. The diminution of the resistivity reduces electric potential gradients in the ionosphere and leads to the formation of field-aligned double layers such that the circulation of the electric field along the whole circuit is equal to zero (assuming a time independent magnetic field distribution). The field-aligned potential drop accelerates the scattered and precipitating electrons to several keV. An auroral arc is formed by the bombardment of these electrons in the atmosphere. This produces an additional enhancement of the ionospheric conductivity, smaller ionospheric potential differences but larger field-aligned ones. Provided the plasma cloud in the magnetosphere is a large reservoir of electrons or if the cloud is propagating in the $+x$-direction, the source of precipitated electrons is constantly fed and the auroral arc lasts as long as a large EMF is maintained in the magnetotail. This figure is taken from Roth *et al.* (1993).

the electron number densities and temperatures from rocket data showing a discontinuity in the inferred temperatures and densities of the parent magnetospheric plasma at the edge of an auroral arc (Lyons *et al.*, 1979; Lyons, 1981). The ion temperatures were estimated on the premise that ion temperatures in the plasmasheet are typically 4–5 times higher than the electron temperatures. We modeled the electric and plasma structure of the transition layer when the large-scale, externally applied potential across the system is -3.50, -1.65, 0, and $+3.50$ kV. The magnetic field strength deep in the plasmasheet cloud (B_1) was kept equal to 40 nT for all cases.

In the theory of Lyons (1981), the external potential difference ψ_2 is the source of the auroral EMF. Such an additional potential drop will bias the electric potential distribution. It can either sharpen or attenuate the electric potential gradient inside the transition layer as shown in Figure 17. This figure displays the solution for the electric structure of the transition region in the four cases. The left-hand-side panels in Figure 17 characterize the ion-dominated layers, while the right-hand

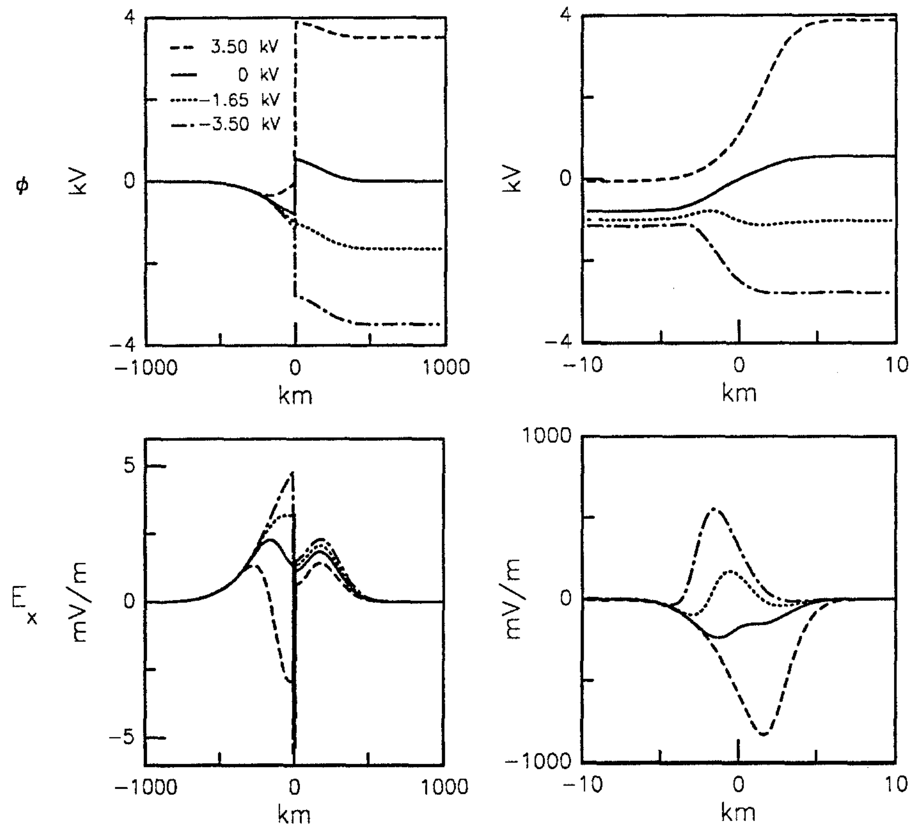

Fig. 17. Electric potential ϕ and electric field E_x structures for different values of the potential difference ($\psi_2 = 3500$ V; 0; -1650 V; -3500 V). The left-hand side panels characterize the ion-dominated layers, located at both ends of the sheath, while the right-hand side panels represent the thin electron-dominated layer near $x = 0$. The presence of a plasma boundary concentrates the imposed electric potential over a small scale size and gives rise to localized potential differences much larger than that produced by the contact between the two plasmas alone (solid curve ψ_2 = 0 V).

panels pertain to the narrow electron-dominated layer near $x \approx 0$. The most striking feature of the potential distributions across these plasma boundaries is that most of the potential difference appears over a small scale size at the boundary. The presence of plasma boundaries in the system concentrates imposed electric fields and gives rise to localized potential differences much larger than that produced by the contact between the two plasmas alone. The actual potential differences available in the magnetosphere because of the solar wind's interaction with the geomagnetic field often exceed 100 kV, but the exact value will depend on the amount of intervening structure between the magnetotail boundary layer and the solar wind. Furthermore, the plasmas in the outer magnetosphere are known to be highly structured with both large-scale structures (e.g., the boundary layer of the plasma sheet) and small-scale internal structures (e.g., illustrated in Parks *et al.*, 1992).

Lyons (1981) has demonstrated that the existence of a large potential difference applied over a small scale size transverse to the magnetic field in the outer magnetosphere is a sufficient condition for the creation of large magnetic field-aligned potential differences between the outer magnetosphere and the ionosphere so as to accelerate electrons downwards. Any magnetospheric electrons scattered into the atmospheric loss cone will be energized and precipitated to produce aurorae.

The plasma populations within the transition region are likely to produce a wide variety of waves which can scatter the electrons into the atmospheric loss cone. Moreover, the modeled scale sizes of the potential distributions transverse to the magnetic field in the outer magnetosphere are no greater than 500-800 km and exhibit structure on even smaller dimensions. Such scale sizes map from the outer magnetosphere to dimensions of tens of km at ionospheric altitudes, dimensions consistent with those of auroral displays. Because the scale size of the transition regions between plasmas is appropriate to auroral arc dimensions, because the electric potential differences across such boundaries are consistent with those required to account for the energized electrons associated with discrete auroral arcs (much enhanced by the large-scale potentials applied across the magnetosphere), and because wave particle interactions within the transition regions likely produce pitch angle scattering we conclude that plasma boundaries are the location and source of electromotive force required to produce discrete aurorae.

10. Multi-species TDs in the Solar Wind

So far, only plasmas consisting of electrons and protons have been considered. In the solar wind, however, the presence of heavier ions may alter the structure of the discontinuity. The modeling of directional discontinuities in a multi-species plasma is part of the Interdisciplinary Study of Directional Discontinuities in the Solar Wind in the framework of the ULYSSES Mission (Lemaire *et al.*, 1983). One objective of this study is a detailed comparison of theoretical calculations with magnetic field and particle flux measurements performed by instruments onboard the ULYSSES spacecraft. The best time resolution of magnetic field measurements obtained with the ULYSSES spacecraft (2 vectors by second) (Balogh *et al.*, 1983) is sufficient to resolve the structure of not too sharp discontinuities (with large thickness, of the order of several proton Larmor radii). Although the best time resolution for direct plasma measurements is much lower, a selection of TDs in the solar wind can be made where, on both sides of these selected cases, first moments of the velocity distributions have been clearly determined from observations. Here, an example from Roth (1986, Figures 1, 2, and 3) is discussed that includes electrons, protons and alpha particles. This example is based on typical plasma data found in the solar wind, not on specific measurements of plasma and field across an observed TD.

There are no inner populations in the simulation summarized by Table IX. The transition is a region where two outer plasmas with three components interpenetrate.

TABLE IX
A solar wind TD

Reference parameters and boundary conditions										
	T_0 eV	B_0 nT	k_1	k_2	ψ_2 V	x_0^*	B_1 nT	θ_0 °	a_{0y}^*	a_{0z}^*
protons	6	4.95	3	2	0	−23	4.95	45	−15	−15

Plasma populations									
	N cm^{-3}	T eV	$\mathcal{U}_y$ km s^{-1}	$\mathcal{U}_z$ km s^{-1}	C_i	L_y	L_z	p_{0y}^*	p_{0z}^*
Outer left populations									
Electrons	5.00	15	218.6	−310.7	1 1 1 1	–	–	–	–
Protons	4.50	6	222.9	−315.0	1 0 1 1	1	1	0	0
Alpha particles	0.25	16	179.7	−271.8	1 0 1 1	1.63	1.63	0	0
Outer right populations									
Electrons	3.00	10	175	−285	1 1 1 1	–	–	–	–
Protons	2.70	4	175	−285	0 1 0 0	0.82	0.82	0	0
Alpha particles	0.15	12	175	−285	0 1 0 0	1.41	1.41	5	5

Typical plasma boundary conditions were chosen. On side 1, for negative values of x, there is a 'hot' plasma of hydrogen and helium, while on side 2, for positive values of x, there is a 'cold' plasma of hydrogen and helium. Notice that each plasma component on side 1 has a distinct partial velocity satisfying Equations (16) and (17) for $j = 1$. The partial velocities on side 2 are equal to the plasma bulk velocity in Equation (26). The values of the normalized thicknesses (L_y and L_z) in Table IX correspond to velocity distribution functions of Sestero type. Each electron velocity distribution function is isotropic about its mean velocity. The electric potential difference ψ_2 is set to zero in this simulation.

Figure 18 displays the structure of the discontinuity. The plasma characteristics of species originating from side 1 and side 2 are illustrated in the four panels on the left-hand side, and in the four central panels, respectively. The four panels on the right-hand side refer to the admixture of the two outer plasmas. Figure 19 summarizes the electric and magnetic structure.

The results in Figures 18 and 19 show how to model a tangential discontinuity in a multi-species solar wind plasma, with shears in both the flow velocity and magnetic field.

Recently we have attempted to model a broad tangential discontinuity based on actual ULYSSES observations on July 3, 1993, 5:29 UT, at 4.57 AU and −33.8°

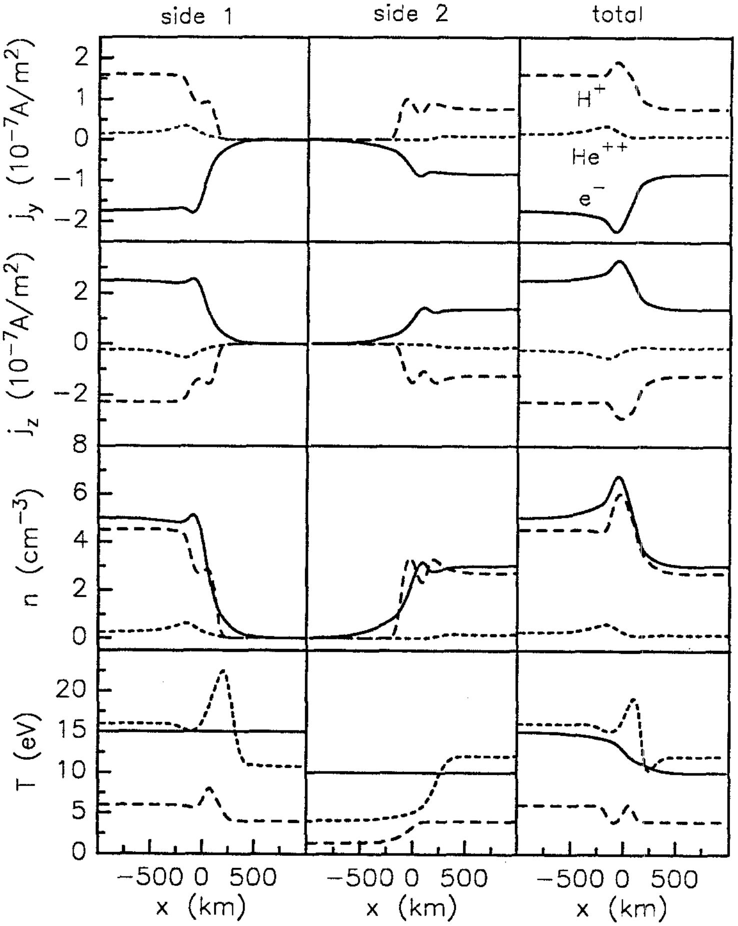

Fig. 18. The plasma in a multi-species solar wind TD. Labels e, H and He refer to electron, proton and alpha particle populations. Side 1 corresponds to $x = -\infty$, side 2 to $x = +\infty$.

heliographic latitude (De Keyser *et al.*, 1995). Its width is about 130 000 km, corresponding to 230 proton gyroradii. Dashed lines on Figure 20 show the magnetic field components in the minimum variance frame; the solid lines depict the simulated profile. The model can represent the overall multi-layer structure of this TD fairly well. The success of such a simulation confirms that our kinetic model constitutes a realistic basis for further studies of the structure and stability of tangential discontinuities.

11. Discussion

Extensive theoretical work has been performed on the equilibrium structure of TDs by constructing steady state solutions of the Vlasov equation. In the multi-

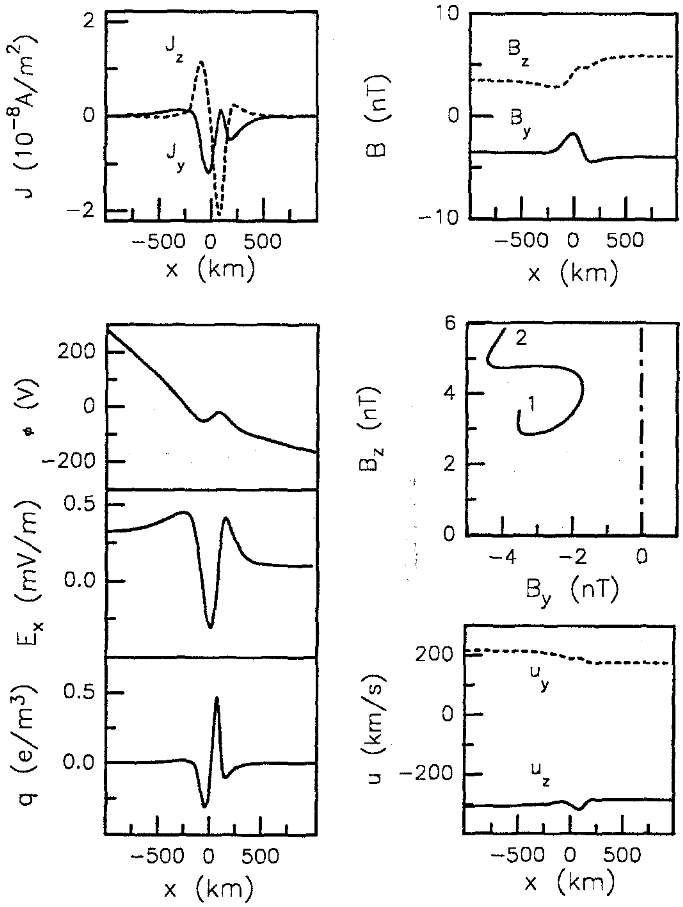

Fig. 19. The electromagnetic structure of a multi-species solar wind TD; hodograms and plasma flow profiles.

species model presented in this review all particle populations (from both outer regions and from inside the layer) are described using a unique formalism for the velocity distribution functions. We have demonstrated in this review that most of the previous models found in the literature can be retrieved as special cases of our general model. Our model also describes current layers with velocity shear and large angles of magnetic field rotation. It can therefore be applied to very complex structures often observed, e.g., at the magnetopause or at the heliospheric current sheet. Such a multi-species model with a large number of free parameters and different gradient scales can illustrate many observable features of TDs, including their multiscale fine structure. However, the one-dimensional, time-independent Vlasov approach has a number of limitations:

– The one-dimensional assumption generally used in these models implies that the TD is of infinite extent in the y and z direction. However, with a magnetopause

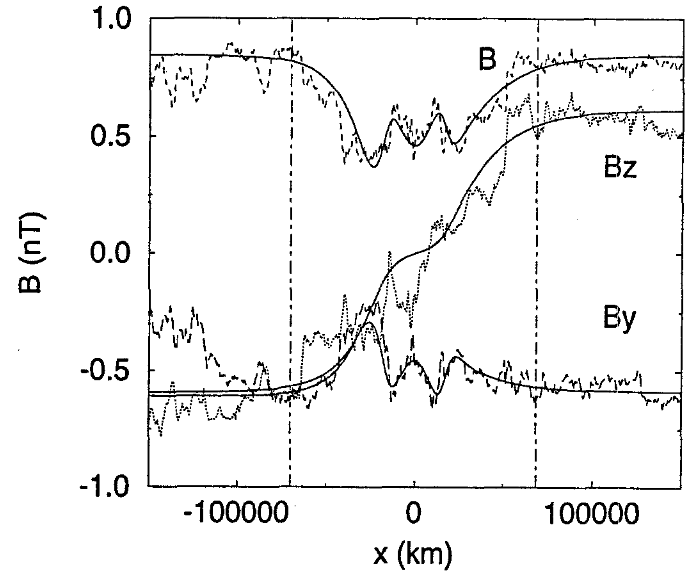

Fig. 20. Observed (dashed lines) and simulated (solid lines) magnetic field components in the MVF (rotated for convenience by $-15°$ along the x-axis) for a solar wind TD observed by ULYSSES. The average normal field (not shown) does not exceed 15 % of the field magnitude. The vertical lines delimit the TD crossing, centered at July 3, 5:29 UT, and lasting about 3 min. The horizontal axis gives the corresponding length scale along the TD normal (magnetic field data courtesy: A. Balogh, Imperial College, U.K.).

thickness of the order of 1000 km (Berchem and Russell, 1982a) and a radius of curvature of a few $R_\oplus$, the one-dimensional assumption is reasonable. The radius of curvature in the solar wind can exceed 10^6 km, so the one-dimensional approach may be even better.

– Vlasov theories of plane tangential discontinuities yield nonunique solutions, as particle distribution functions can be assigned arbitrarily to different regions of phase space. For convenience only single-valued distribution functions of the constants of motion are considered.

– Time-independent plane TD models do not provide a complete solution to the problem of particle accessibility, both to the current layer itself, and, more specifically, to different phase space regions (Whipple *et al.*, 1984). In purely plane and stationary models, all the particles are essentially trapped in the sense that none come from or can go to arbitrarily large distances from the current layer, and we therefore have no information about drift paths that go back to the particle source. It is also necessary to know something about the drift paths in order to locate the particles in phase space, and to determine the demarcation boundaries between the plasmas that originate in different source regions. Stationary plane Vlasov configurations are supposed to be formed from remote plasma source regions by suitable transport across magnetic field lines. A possible way to solve the particle accessibility problem is to consider the temporal behavior of the sheath (Morse,

1965) and/or two or three-dimensional models. Full or hybrid particle simulations are different approaches to TD structure; the basic premise of these approaches is that useful information about TDs can be obtained by studying their temporal evolution starting from an initial state (Berchem and Okuda, 1990; Cargill and Eastman, 1991).

– The large number of free parameters obscures the relation between boundary conditions and the internal structure of the layer. The generalized model of TDs presented in this review also introduces a number of free parameters that are not determined by the boundary conditions. Kuznetsova *et al.* (1995) have discussed a procedure that helps to choose appropriate values for all these parameters: among all configurations with the same thickness and boundary conditions, one could select the most stable one, which corresponds to the minimum integrated value of the 'energy levels' of large-scale adiabatic electromagnetic perturbations over the transition. This procedure reduces arbitrariness and allows to determine some properties of the internal structure of the MCL which are not directly measurable (e.g., the electrostatic potential drop across the layer).

– One-dimensional current layers with magnetic shear are thermodynamical nonequilibrium systems that have an excess of free energy and are potentially unstable with respect to the excitation of large-scale perturbations.

Research on the stability of TDs has focussed on the magnetopause because of the availability of observational evidence. Study of magnetopause structure and stability (Section 8) has shown that if the magnetopause thickness is much larger than the marginal one (below which the current layer is subjected to percolation), a large domain of stable magnetic surfaces should exist within it, which should prevent particles diffusion across the layer. Note that microscopic plasma turbulence (e.g., lower hybrid drift instability (Gary and Eastman, 1979; Winske *et al.*, 1995; Treumann *et al.*, 1995) that could provide diffusion when the magnetosheath and magnetospheric fields are parallel) is strongly stabilized by the magnetic shear when θ is substantial. In this case a one-dimensional slab TD could be considered as a good model for the magnetopause current layer if one disregards the question of particle accessibility discussed by Whipple *et al.* (1984). When the thickness is close to the marginal value, the MCL can be modeled as a tangential discontinuity 'spoiled' (in the first approximation) by embedded percolated magnetic filaments. In this case the MCL is likely to have a pore-like fractal structure, where percolated magnetic filaments (common for both sides of the MCL) are surrounded by closed magnetospheric and open magnetosheath field lines. The process of aggregation (self-organization) of these filaments into large-scale clusters (like FTEs) due to the attraction of field aligned currents is a challenging subject for future studies. When the MCL thickness is much less than the marginal one, strong, large-scale magnetic turbulence develops within the layer. The diffusive broadening of the symmetrical current layer when a large number of tearing modes are allowed to grow together was illustrated by Wang and Ashour-Abdalla (1994), using a three-dimensional particle simulation.

Plasma micro-instabilities in TDs have not been considered in this review. These micro-instabilities tend to operate at much higher frequencies than the macro-instabilities. The resulting waves are believed to be generated by currents and beams existing in the TD itself. Currents in TDs can be a considerable fraction of the ion thermal speed, so that relaxation via plasma micro-instabilities could arise. Generation of lower hybrid turbulence is a common feature at the magnetopause (e.g., Anderson *et al.*, 1982). Broadband electrostatic noise is also a common feature observed in the PSBL (Parks *et al.*, 1992). Roth *et al.* (1993) have suggested that this electrostatic noise is a indication that enlarged electron layers (observed scale size 50 km) in the PSBL generate enough wave power to scatter electrons into the loss cone at a rate sufficient to maintain an auroral activity.

Appendix A. Velocity Distribution Moments

In this appendix we analytically compute the moments of the velocity distribution function. Writing

$$
\begin{aligned}
v_x^r v_y^s v_z^t &= (\pm 2)^{r/2} m^{-(r+2s+2t)/2} (H - H_0)^{r/2} (p_y - \frac{Zea_y}{c})^s (p_z - \frac{Zea_z}{c})^t + \\
&\quad + \text{ if } v_x > 0\,, - \text{ if } v_x < 0 \\
&= W(H, p_y, p_z),
\end{aligned}
$$

we have, due to (1) and (7), and because of

$$
\int_{\xi}^{+\infty} (y - \xi)^{(r-1)/2} \exp(-\alpha y)\, \mathrm{d}y = \frac{r!}{(r/2)!2^r} \pi^{1/2} \alpha^{-(r+1)/2} \exp(-\alpha\xi),
$$

that

$$
Q_{rst} = M_{rst} \sum_{k=1}^{4} C_k\, I_{ky}(s)\, I_{kz}(t)
$$

if r is even (it is 0 otherwise), with

$$
\begin{aligned}
M_{rst} &= 2^{-(r+6)/2} \frac{r!}{(r/2)!} m^{-(r+2s+2t+2)/2} \pi^{-1} N\, \mathcal{T}^{(r-2)/2} \times \\
&\quad \times \exp\left[-\frac{1}{\mathcal{T}} (Ze\phi + \tfrac{1}{2} m \mathcal{U}^2) \right],
\end{aligned}
$$

$$I_{ky}(s) = \int_{-\infty}^{+\infty} \left(p_y - \frac{Zea_y}{c}\right)^s \operatorname{erfc}(-\epsilon_{ky} U_y) \times$$

$$\times \exp\left[-\frac{1}{2m\mathcal{T}}\left(p_y - \frac{Zea_y}{c}\right)^2 + \frac{p_y \mathcal{U}_y}{\mathcal{T}}\right] \mathrm{d}p_y,$$

$$I_{kz}(t) = \int_{-\infty}^{+\infty} \left(p_z - \frac{Zea_z}{c}\right)^t \operatorname{erfc}(-\epsilon_{kz} U_z) \times$$

$$\times \exp\left[-\frac{1}{2m\mathcal{T}}\left(p_z - \frac{Zea_z}{c}\right)^2 + \frac{p_z \mathcal{U}_z}{\mathcal{T}}\right] \mathrm{d}p_z,$$

where $\epsilon_k = (\epsilon_{ky}, \epsilon_{kz})$ are the bisectors of the four quadrants of the $(a_y - a_z)$ plane, numbered as:

$$\epsilon_1 = (-1, +1), \quad \epsilon_2 = (+1, +1), \quad \epsilon_3 = (-1, -1), \quad \epsilon_4 = (+1, -1).$$

It is found that (for r even):

$$Q_{rst} = \mathcal{M}_{rst} \sum_{k=1}^{4} C_k \mathcal{I}_{ky}(s) \mathcal{I}_{kz}(t),$$

where

$$\mathcal{M}_{rst} = \frac{1}{4\pi} 2^{-r} \frac{r!}{(r/2)!} N \left(\frac{2\mathcal{T}}{m}\right)^{(r+s+t)/2} \exp\left[-\frac{Ze}{\mathcal{T}}\left(\phi - \frac{a_y}{c}\mathcal{U}_y - \frac{a_z}{c}\mathcal{U}_z\right)\right],$$

$$\mathcal{I}_{ky}(s) = \int_{-\infty}^{+\infty} \exp(-p_y^2)(p_y - K_y)^s \operatorname{erfc}(A_{ky} p_y + B_{ky}) \, \mathrm{d}p_y, \tag{A.1}$$

$$\mathcal{I}_{kz}(t) = \int_{-\infty}^{+\infty} \exp(-p_z^2)(p_z - K_z)^t \operatorname{erfc}(A_{kz} p_z + B_{kz}) \, \mathrm{d}p_z, \tag{A.2}$$

where we used the abbreviations:

$$K_y = -\left(\frac{m}{2\mathcal{T}}\right)^{1/2} \mathcal{U}_y, \qquad K_z = -\left(\frac{m}{2\mathcal{T}}\right)^{1/2} \mathcal{U}_z,$$

$$A_{ky} = -\epsilon_{ky}(2m\mathcal{T})^{1/2}\delta_y, \qquad A_{kz} = -\epsilon_{kz}(2m\mathcal{T})^{1/2}\delta_z,$$

$$B_{ky} = -\epsilon_{ky}\delta_y\left(Ze\frac{a_y}{c} - hp_{0y}\right), \qquad B_{kz} = -\epsilon_{kz}\delta_z\left(Ze\frac{a_z}{c} - hp_{0z}\right).$$

The integrals (A.1) and (A.2) are both of the form:

$$I_n(\kappa, \alpha, \beta) = \int_{-\infty}^{+\infty} \exp(-y^2)(y-\kappa)^n \operatorname{erfc}(\alpha y + \beta)\, \mathrm{d}y.$$

With the binomial expansion, we find:

$$I_n(\kappa, \alpha, \beta) = \sum_{k=0}^{n} \frac{n!}{k!(n-k)!}(-\kappa)^{n-k} J_k(\alpha, \beta),$$

$$J_k(\alpha, \beta) = \int_{-\infty}^{+\infty} \exp(-y^2)\, y^k \operatorname{erfc}(\alpha y + \beta)\, \mathrm{d}y.$$

Any moment of order $r+s+t$ can now be calculated. In particular, for moments of order not greater than 2, which include most plasma parameters of interest, it suffices to calculate J_0, J_1, J_2, I_0, I_1, I_2:

$$J_0(\alpha, \beta) = \sqrt{\pi} \operatorname{erfc}(\mathcal{R}),$$

$$J_1(\alpha, \beta) = -\mathcal{S} \exp(-\mathcal{R}^2),$$

$$J_2(\alpha, \beta) = \frac{\sqrt{\pi}}{2} \operatorname{erfc}(\mathcal{R}) + \mathcal{R}\mathcal{S}^2 \exp(-\mathcal{R}^2),$$

$$I_0(\kappa, \alpha, \beta) = \sqrt{\pi} \operatorname{erfc}(\mathcal{R}),$$

$$I_1(\kappa, \alpha, \beta) = -\sqrt{\pi}\kappa \operatorname{erfc}(\mathcal{R}) - \mathcal{S} \exp(-\mathcal{R}^2),$$

$$I_2(\kappa, \alpha, \beta) = \sqrt{\pi}\,(\kappa^2 + \tfrac{1}{2}) \operatorname{erfc}(\mathcal{R}) + \mathcal{S}(2\kappa + \mathcal{S}\mathcal{R}) \exp(-\mathcal{R}^2),$$

where

$$\mathcal{R} = \beta(1+\alpha^2)^{-1/2}, \quad \mathcal{S} = \alpha(1+\alpha^2)^{-1/2}.$$

Introducing

$$\mathcal{A}_y = \frac{1}{l_y \rho B_0}\left(a_y - \frac{c p_{0y}}{|Z|e}\right), \quad \mathcal{A}_z = \frac{1}{l_z \rho B_0}\left(a_z - \frac{c p_{0z}}{|Z|e}\right),$$

$$\rho B_0 = \frac{c\sqrt{2m\mathcal{T}}}{|Z|e},$$

it can be seen that:

$$\mathcal{R}_{ky} = B_{ky}(1 + A_{ky}^2)^{-1/2} = -\epsilon_{ky}\mathcal{A}_y,$$

$$\mathcal{R}_{kz} = B_{kz}(1 + A_{kz}^2)^{-1/2} = -\epsilon_{kz}\mathcal{A}_z,$$

$$\mathcal{S}_{ky} = A_{ky}(1 + A_{ky}^2)^{-1/2} = -\epsilon_{ky}h/l_y,$$

$$\mathcal{S}_{kz} = A_{kz}(1 + A_{kz}^2)^{-1/2} = -\epsilon_{kz}h/l_z.$$

We then obtain:

$$\mathcal{I}_{ky}(0)=\sqrt{\pi}\,\mathrm{erfc}(-\epsilon_{ky}\mathcal{A}_y),$$
$$\mathcal{I}_{ky}(1)=\sqrt{\pi}\,\underline{\mathcal{U}}_y\,\mathrm{erfc}(-\epsilon_{ky}\mathcal{A}_y) + \frac{\epsilon_{ky}h}{l_y}\,\exp(-\mathcal{A}_y^2),$$
$$\mathcal{I}_{ky}(2)=\frac{\sqrt{\pi}}{2}(1 + 2\underline{\mathcal{U}}_y^2)\mathrm{erfc}(-\epsilon_{ky}\mathcal{A}_y) + \epsilon_{ky}\left(\frac{2h\underline{\mathcal{U}}_y}{l_y} - \frac{\mathcal{A}_y}{l_y^2}\right)\exp(-\mathcal{A}_y^2),$$
$$\mathcal{I}_{kz}(0)=\sqrt{\pi}\,\mathrm{erfc}(-\epsilon_{kz}\mathcal{A}_z),$$
$$\mathcal{I}_{kz}(1)=\sqrt{\pi}\,\underline{\mathcal{U}}_z\,\mathrm{erfc}(-\epsilon_{kz}\mathcal{A}_z) + \frac{\epsilon_{kz}h}{l_z}\,\exp(-\mathcal{A}_z^2),$$
$$\mathcal{I}_{kz}(2)=\frac{\sqrt{\pi}}{2}(1 + 2\underline{\mathcal{U}}_z^2)\mathrm{erfc}(-\epsilon_{kz}\mathcal{A}_z) + \epsilon_{kz}\left(\frac{2h\underline{\mathcal{U}}_z}{l_z} - \frac{\mathcal{A}_z}{l_z^2}\right)\exp(-\mathcal{A}_z^2),$$

where

$$\underline{\mathcal{U}}_y = \frac{\mathcal{U}_y}{\sqrt{2\mathcal{T}/m}}, \quad \underline{\mathcal{U}}_z = \frac{\mathcal{U}_z}{\sqrt{2\mathcal{T}/m}}.$$

We now find analytical expressions for the first moments:

$$Q_{000} = N\exp\left(-\frac{Ze}{\mathcal{T}}\varphi\right)G(\mathcal{A}_y, \mathcal{A}_z),$$

$$Q_{010} = N\left(\frac{2\mathcal{T}}{m}\right)^{1/2}\exp\left(-\frac{Ze}{\mathcal{T}}\varphi\right)\times$$
$$\times\left[\underline{\mathcal{U}}_y G(\mathcal{A}_y, \mathcal{A}_z) + \frac{1}{\sqrt{\pi}}\frac{h}{l_y}\mathcal{Y}(\mathcal{A}_z)\,\exp(-\mathcal{A}_y^2)\right],$$

$$Q_{001} = N\left(\frac{2\mathcal{T}}{m}\right)^{1/2}\exp\left(-\frac{Ze}{\mathcal{T}}\varphi\right)\times$$
$$\times\left[\underline{\mathcal{U}}_z G(\mathcal{A}_y, \mathcal{A}_z) + \frac{1}{\sqrt{\pi}}\frac{h}{l_z}\mathcal{Z}(\mathcal{A}_y)\,\exp(-\mathcal{A}_z^2)\right],$$

$$Q_{200} = \frac{\mathcal{T}}{m}N\exp\left(-\frac{Ze}{\mathcal{T}}\varphi\right)G(\mathcal{A}_y, \mathcal{A}_z) = \frac{\mathcal{T}}{m}Q_{000},$$

$$Q_{020}=N\frac{2\mathcal{T}}{m}\exp\left(-\frac{Ze}{\mathcal{T}}\varphi\right)\left[\frac{1}{2}\left(1+2\underline{\mathcal{U}}_y^2\right)G(\mathcal{A}_y,\mathcal{A}_z)+\right.$$
$$\left.+\frac{h}{\sqrt{\pi}l_y}\left(2\underline{\mathcal{U}}_y-h\frac{\mathcal{A}_y}{l_y}\right)\mathcal{Y}(\mathcal{A}_z)\exp(-\mathcal{A}_y^2)\right],$$

$$Q_{002}=N\frac{2\mathcal{T}}{m}\exp\left(-\frac{Ze}{\mathcal{T}}\varphi\right)\left[\frac{1}{2}\left(1+2\underline{\mathcal{U}}_z^2\right)G(\mathcal{A}_y,\mathcal{A}_z)+\right.$$
$$\left.+\frac{h}{\sqrt{\pi}l_z}\left(2\underline{\mathcal{U}}_z-h\frac{\mathcal{A}_z}{l_z}\right)\mathcal{Z}(\mathcal{A}_y)\exp(-\mathcal{A}_z^2)\right],$$

where

$$\varphi = \phi-\frac{a_y\mathcal{U}_y+a_z\mathcal{U}_z}{c},$$
$$G(\mathcal{A}_y,\mathcal{A}_z)=\frac{1}{4}\sum_{k=1}^{4}C_k\,\mathrm{erfc}(-\epsilon_{ky}\mathcal{A}_y)\,\mathrm{erfc}(-\epsilon_{kz}\mathcal{A}_z), \tag{A.3}$$
$$\mathcal{Z}(\mathcal{A}_y)=\frac{1}{4}\sum_{k=1}^{4}\epsilon_{kz}C_k\,\mathrm{erfc}(-\epsilon_{ky}\mathcal{A}_y)=$$
$$=\tfrac{1}{4}(C_1-C_3)\,\mathrm{erfc}(+\mathcal{A}_y)+\tfrac{1}{4}(C_2-C_4)\,\mathrm{erfc}(-\mathcal{A}_y),$$
$$\mathcal{Y}(\mathcal{A}_z)=\frac{1}{4}\sum_{k=1}^{4}\epsilon_{ky}C_k\,\mathrm{erfc}(-\epsilon_{kz}\mathcal{A}_z)=$$
$$=\tfrac{1}{4}(C_4-C_3)\,\mathrm{erfc}(+\mathcal{A}_z)+\tfrac{1}{4}(C_2-C_1)\,\mathrm{erfc}(-\mathcal{A}_z).$$

The plasma parameters can now be calculated explicitly. First notice that:

$$N\left(\frac{2\mathcal{T}}{m}\right)^{1/2}\exp\left(-\frac{Ze}{\mathcal{T}}\varphi\right)\frac{1}{\sqrt{\pi}}\frac{h}{l_y}\mathcal{Y}(\mathcal{A}_z)\exp(-\mathcal{A}_y^2)=$$
$$=Q_{010}-\left(\frac{2\mathcal{T}}{m}\right)^{1/2}\underline{\mathcal{U}}_yQ_{000}=\left(\frac{2\mathcal{T}}{m}\right)^{1/2}(\underline{u}_y-\underline{\mathcal{U}}_y)Q_{000},$$

$$N\left(\frac{2\mathcal{T}}{m}\right)^{1/2}\exp\left(-\frac{Ze}{\mathcal{T}}\varphi\right)\frac{1}{\sqrt{\pi}}\frac{h}{l_z}\mathcal{Z}(\mathcal{A}_y)\exp(-\mathcal{A}_z^2)=$$
$$=Q_{001}-\left(\frac{2\mathcal{T}}{m}\right)^{1/2}\underline{\mathcal{U}}_zQ_{000}=\left(\frac{2\mathcal{T}}{m}\right)^{1/2}(\underline{u}_z-\underline{\mathcal{U}}_z)Q_{000},$$

$$Q_{020}=\frac{\mathcal{T}}{m}\left[1-2(\underline{\mathcal{U}}_y-\underline{u}_y)\left(\underline{\mathcal{U}}_y-h\frac{\mathcal{A}_y}{l_y}\right)+2\underline{\mathcal{U}}_y\underline{u}_y\right]Q_{000},$$

$$Q_{002} = \frac{\mathcal{T}}{m}\left[1 - 2(\underline{\mathcal{U}}_z - \underline{u}_z)\left(\underline{\mathcal{U}}_z - h\frac{\mathcal{A}_z}{l_z}\right) + 2\underline{\mathcal{U}}_z\underline{u}_z\right] Q_{000},$$

where

$$\underline{u}_y = \frac{u_y}{\sqrt{2\mathcal{T}/m}}, \quad \underline{u}_z = \frac{u_z}{\sqrt{2\mathcal{T}/m}}.$$

One can then deduce:

$$n = N \exp\left(-\frac{Ze}{\mathcal{T}}\varphi\right) G(\mathcal{A}_y, \mathcal{A}_z), \tag{A.4}$$

$$j_y = Ze\left\{n\mathcal{U}_y + N\left(\frac{2\mathcal{T}}{m}\right)^{1/2} \exp\left(-\frac{Ze}{\mathcal{T}}\varphi\right)\frac{1}{\sqrt{\pi}}\frac{h}{l_y}\mathcal{Y}(\mathcal{A}_z)\exp(-\mathcal{A}_y^2)\right\},$$

$$j_z = Ze\left\{n\mathcal{U}_z + N\left(\frac{2\mathcal{T}}{m}\right)^{1/2} \exp\left(-\frac{Ze}{\mathcal{T}}\varphi\right)\frac{1}{\sqrt{\pi}}\frac{h}{l_z}\mathcal{Z}(\mathcal{A}_y)\exp(-\mathcal{A}_z^2)\right\},$$

$$\begin{aligned}
T_x &= \mathcal{T}, \\
T_y &= \mathcal{T}\left[1 - 2(\underline{\mathcal{U}}_y - \underline{u}_y)^2 + 2(\underline{\mathcal{U}}_y - \underline{u}_y)h\frac{\mathcal{A}_y}{l_y}\right], \\
T_z &= \mathcal{T}\left[1 - 2(\underline{\mathcal{U}}_z - \underline{u}_z)^2 + 2(\underline{\mathcal{U}}_z - \underline{u}_z)h\frac{\mathcal{A}_z}{l_z}\right],
\end{aligned}$$

with

$$\underline{u}_y = \underline{\mathcal{U}}_y + \frac{1}{\sqrt{\pi}}\frac{h}{l_y}\frac{\mathcal{Y}(\mathcal{A}_z)\exp(-\mathcal{A}_y^2)}{G(\mathcal{A}_y, \mathcal{A}_z)},$$

$$\underline{u}_z = \underline{\mathcal{U}}_z + \frac{1}{\sqrt{\pi}}\frac{h}{l_z}\frac{\mathcal{Z}(\mathcal{A}_y)\exp(-\mathcal{A}_z^2)}{G(\mathcal{A}_y, \mathcal{A}_z)}.$$

Appendix B. Scaling Factors

In this Appendix we introduce reference values for all physical quantities. We select a reference particle with mass $\lambda_m = m_0$, degree of ionization Z_0, and thermal energy $\mathcal{T}_0$. We also choose a reference magnetic field B_0. The scaling factors can then be defined as:

– *Velocity*: the perpendicular thermal velocity v_0 of the reference particles,

$$\lambda_V = v_0 = \sqrt{\frac{2\mathcal{T}_0}{m_0}}. \tag{B.1}$$

– *Length*: the Larmor radius ρ_0 of the reference particle in field B_0,

$$\lambda_{\mathcal{L}} = \rho_0 = \frac{m_0 v_0 c}{|Z_0|eB_0} = \frac{c\sqrt{2m_0\mathcal{T}_0}}{|Z_0|eB_0}. \tag{B.2}$$

– *Magnetic and electric field*: In the Gaussian system, the electric and magnetic fields have the same units; therefore:

$$\lambda_E = \lambda_B = B_0. \tag{B.3}$$

– *Electric and magnetic potentials*: from (B.2) and (B.3):

$$\lambda_\phi = \lambda_a = \frac{m_0 v_0 c}{|Z_0|e}.$$

– *Charge*: because $\lambda_e\lambda_a/\lambda_V$ represents a momentum ($\lambda_m\lambda_V$), we have

$$\lambda_e = \lambda_m\lambda_V^2/\lambda_a = \frac{|Z_0|ev_0}{c}.$$

– *Time* and *current density*: because of Maxwell's equation

$$\nabla \times \mathbf{B} = \frac{1}{c}\frac{\partial \mathbf{E}}{\partial t} + \frac{4\pi}{c}\mathbf{J},$$

we have $\lambda_t = \lambda_{\mathcal{L}}/\lambda_V$ and $\lambda_J = \lambda_V\lambda_B/\lambda_{\mathcal{L}}$:

$$\lambda_t = \frac{m_0 c}{|Z_0|eB_0}, \quad \lambda_J = \frac{|Z_0|eB_0^2}{m_0 c}.$$

λ_t is the Larmor period of reference particles in magnetic field B_0.

– *Energy*: because $\lambda_e\lambda_\phi$ represents an electrostatic energy, we have

$$\lambda_{\mathcal{T}} = 2\mathcal{T}_0$$

– *Particle number density*: because $\lambda_J = \lambda_n\lambda_e\lambda_V$, we have:

$$\lambda_n = \frac{B_0^2}{m_0 v_0^2} = \frac{B_0^2}{2\mathcal{T}_0}.$$

– *Pressure*: we can deduce the unit of pressure from either the magnetic pressure ($B^2/8\pi$) or the plasma partial pressure ($\mathcal{P}^\nu = n^\nu \mathcal{T}^\nu$):

$$\lambda_{\mathcal{P}} = B_0^2.$$

– *Charge density*: from $\nabla \cdot \mathbf{E} = 4\pi q$ or from $q = \sum Zne$ it is found that

$$\lambda_q = \lambda_{\phi''} = \frac{|Z_0|eB_0^2}{m_0 v_0 c}.$$

Appendix C. Electric Field and Charge Density

Taking the derivative of the charge neutrality Equation (32) with respect to x yields a relation between the electric and magnetic fields:

$$E_x(x) = \left(B_z \sum_{\nu=1}^{s} Z^\nu \frac{\mathrm{d}n^\nu}{\mathrm{d}a_y} - B_y \sum_{\nu=1}^{s} Z^\nu \frac{\mathrm{d}n^\nu}{\mathrm{d}a_z} \right) \Big/ \sum_{\nu=1}^{s} Z^\nu \frac{\mathrm{d}n^\nu}{\mathrm{d}\phi}.$$

In Appendix A the moments of the distribution function, like $n(x)$, are expressed in terms of the quantities $\mathcal{A}_y$, $\mathcal{A}_z$, and φ. This allows us to compute (dropping the ν index):

$$\frac{\mathrm{d}n}{\mathrm{d}\phi} = -\frac{Ze}{\mathcal{T}} n(x),$$

$$\frac{\mathrm{d}n}{\mathrm{d}a_y} = \frac{Ze\mathcal{U}_y}{c\mathcal{T}} n(x) + \frac{N}{L_y \rho_0 B_0} \exp\left(-\frac{Ze}{\mathcal{T}}\varphi\right) \frac{\mathrm{d}G}{\mathrm{d}\mathcal{A}_y},$$

$$\frac{\mathrm{d}n}{\mathrm{d}a_z} = \frac{Ze\mathcal{U}_z}{c\mathcal{T}} n(x) + \frac{N}{L_z \rho_0 B_0} \exp\left(-\frac{Ze}{\mathcal{T}}\varphi\right) \frac{\mathrm{d}G}{\mathrm{d}\mathcal{A}_z},$$

$$\frac{\mathrm{d}G}{\mathrm{d}\mathcal{A}_y} = \frac{2}{\sqrt{\pi}} \exp(-\mathcal{A}_y^2)\mathcal{Y}(\mathcal{A}_z),$$

$$\frac{\mathrm{d}G}{\mathrm{d}\mathcal{A}_z} = \frac{2}{\sqrt{\pi}} \exp(-\mathcal{A}_z^2)\mathcal{Z}(\mathcal{A}_y).$$

The charge density distribution $q(x) = \sum_{\nu=1}^{s} Z^\nu e n^\nu$ is obtained from Poisson's equation:

$$\frac{\mathrm{d}^2\phi}{\mathrm{d}x^2} = -4\pi q(x).$$

The Laplacian of ϕ can be calculated as a function of ϕ, a_y and a_z, by taking the second derivative of the charge neutrality Equation (32). After some algebra, we see that:

$$
\begin{aligned}
q = & -\frac{1}{4\pi e \sum_{\nu=1}^{s} (Z^\nu)^2 n^\nu / \mathcal{T}^\nu} \times \\
& \times \left\{ 2E_x B_y \sum_{\nu=1}^{s} Z^\nu \frac{\mathrm{d}^2 n^\nu}{\mathrm{d}\phi \mathrm{d}a_z} - 2E_x B_z \sum_{\nu=1}^{s} Z^\nu \frac{\mathrm{d}^2 n^\nu}{\mathrm{d}\phi \mathrm{d}a_y} + E_x^2 \sum_{\nu=1}^{s} Z^\nu \frac{\mathrm{d}^2 n^\nu}{\mathrm{d}\phi^2} + \right. \\
& + B_y^2 \sum_{\nu=1}^{s} Z^\nu \frac{\mathrm{d}^2 n^\nu}{\mathrm{d}a_z^2} + B_z^2 \sum_{\nu=1}^{s} Z^\nu \frac{\mathrm{d}^2 n^\nu}{\mathrm{d}a_y^2} - 2B_y B_z \sum_{\nu=1}^{s} Z^\nu \frac{\mathrm{d}^2 n^\nu}{\mathrm{d}a_y \mathrm{d}a_z} - \\
& \left. - \frac{4\pi}{c} J_y \sum_{\nu=1}^{s} Z^\nu \frac{\mathrm{d}n^\nu}{\mathrm{d}a_y} - \frac{4\pi}{c} J_z \sum_{\nu=1}^{s} Z^\nu \frac{\mathrm{d}n^\nu}{\mathrm{d}a_z} \right\},
\end{aligned}
$$

where (dropping the ν index):

$$
\frac{\mathrm{d}^2 n}{\mathrm{d}\phi \mathrm{d}a_z} = -\frac{Z^2 e^2 \mathcal{U}_z}{\mathcal{T}^2 c} n - \frac{ZeN}{L_z \rho_0 B_0 \mathcal{T}} \exp\left(-\frac{Ze}{\mathcal{T}} \varphi\right) \frac{\mathrm{d}G}{\mathrm{d}\mathcal{A}_z},
$$

$$
\frac{\mathrm{d}^2 n}{\mathrm{d}\phi \mathrm{d}a_y} = -\frac{Z^2 e^2 \mathcal{U}_y}{\mathcal{T}^2 c} n - \frac{ZeN}{L_y \rho_0 B_0 \mathcal{T}} \exp\left(-\frac{Ze}{\mathcal{T}} \varphi\right) \frac{\mathrm{d}G}{\mathrm{d}\mathcal{A}_y},
$$

$$
\frac{\mathrm{d}^2 n}{\mathrm{d}\phi^2} = \frac{Z^2 e^2}{\mathcal{T}^2} n,
$$

$$
\frac{\mathrm{d}^2 n}{\mathrm{d}a_z^2} = \left(\frac{Ze\mathcal{U}_z}{c\mathcal{T}}\right)^2 n + \frac{2N}{L_z \rho_0 B_0} \left(\frac{Ze\mathcal{U}_z}{c\mathcal{T}} - \frac{\mathcal{A}_z}{L_z \rho_0 B_0}\right) \exp\left(-\frac{Ze}{\mathcal{T}} \varphi\right) \frac{\mathrm{d}G}{\mathrm{d}\mathcal{A}_z},
$$

$$
\frac{\mathrm{d}^2 n}{\mathrm{d}a_y^2} = \left(\frac{Ze\mathcal{U}_y}{c\mathcal{T}}\right)^2 n + \frac{2N}{L_y \rho_0 B_0} \left(\frac{Ze\mathcal{U}_y}{c\mathcal{T}} - \frac{\mathcal{A}_y}{L_y \rho_0 B_0}\right) \exp\left(-\frac{Ze}{\mathcal{T}} \varphi\right) \frac{\mathrm{d}G}{\mathrm{d}\mathcal{A}_y},
$$

$$
\begin{aligned}
\frac{\mathrm{d}^2 n}{\mathrm{d}a_y \mathrm{d}a_z} = & \left(\frac{Ze}{c\mathcal{T}}\right)^2 \mathcal{U}_y \mathcal{U}_z n + \frac{ZeN}{\rho_0 B_0 c \mathcal{T}} \left(\frac{\mathcal{U}_z}{L_y} \frac{\mathrm{d}G}{\mathrm{d}\mathcal{A}_y} + \frac{\mathcal{U}_y}{L_z} \frac{\mathrm{d}G}{\mathrm{d}\mathcal{A}_z}\right) \exp\left(-\frac{Ze}{\mathcal{T}} \varphi\right) + \\
& + \frac{N}{\pi L_y L_z \rho_0^2 B_0^2} (C_2 + C_3 - C_1 - C_4) \exp\left[-\left(\frac{Ze}{\mathcal{T}} \varphi + \mathcal{A}_y^2 + \mathcal{A}_z^2\right)\right].
\end{aligned}
$$

Acknowledgements

M.R. wishes to express his special thanks to Prof. M. Nicolet for his long-term personal support and encouragements. M.R. also thanks D. Hubert, C. Lacombe,

S. Hoang, and M. Maksimovic for stimulating discussions about ISEE and ULYSSES observations, and for the warm hospitality of the DESPA laboratory during a stay at the Observatoire de Paris-Meudon. The authors would like to thank D. Evans, J. Lemaire, and B. Tsurutani for fruitful discussions. They are grateful to J. Berchem and C. T. Russell for providing ISEE-1 magnetic field observations, to T. E. Eastman and L. Frank for the corresponding plasma measurements, and to A. Balogh and J. L. Phillips for ULYSSES data. J.D.K. and M.R. are supported by the ESA (PRODEX) project 'Interdisciplinary Study of Directional Discontinuities' as part of the ULYSSES mission, and acknowledge the support of the Belgian Services for Scientific, Technological and Cultural Affairs. M.R. thanks the Belgian National Fund for Scientific Research for a research grant. M.M.K. gratefully acknowledges support by the US NRC. The authors are also grateful to M. Ackerman, Director of the Belgian Institute for Space Aeronomy, for his support.

References

Alfvén, H.: 1981, *Cosmic Plasma*, D. Reidel Publ. Co., Dordrecht, Holland.

Alpers W.: 1969, 'Steady State Charge Neutral Models of the Magnetopause', *Astrophys. Space Sci.* **5**, 425.

Anderson, R. R., Harvey, C. C., Hoppe, M. M., Tsurutani, B. T., Eastman, T. E., and Etcheto, J.: 1982, 'Plasma Waves Near the Magnetopause', *J. Geophys. Res.* **87**, 2087.

Balogh, A., Hedgecock, P. C., Smith, E. J., and Tsurutani, B. T.: 1983, 'The Magnetic Field Investigation on ISPM' in K.-P. Wenzel, R. G. Marsden, and B. Battrick, ed(s)., *The International Solar Polar Mission —Its Scientific Investigations*, European Space Agency, ESA SP-1050, p. 27.

Behannon, K. W., Neubauer, F. M., and Barnstorf, H.: 1981, 'Fine-Scale Characteristics of Interplanetary Sector Boundaries', *J. Geophys. Res.* **86**, 3273.

Berchem, J. and Okuda, H.: 1990, 'A Two-Dimensional Particle Simulation of the Magnetopause Current Layer', *J. Geophys. Res.* **95**, 8133.

Berchem, J. and Russell, C. T.: 1982a, 'The Thickness of the Magnetopause Current Layer: ISEE 1 and 2 Observations', *J. Geophys. Res.* **87**, 2108.

Berchem, J. and Russell, C.T.: 1982b, 'Magnetic Field Rotation through the Magnetopause: ISEE 1 and 2 Observations', *J. Geophys. Res.* **87**, 8139.

Berchem, J. and Russell, C.T.: 1984, 'Flux Transfer Events on the Magnetopause: Spatial Distributions and Controlling Factors', *J. Geophys. Res.* **89**, 6689.

Burlaga, L. F., Lemaire, J. F., and Turner, J. M.: 1977, 'Interplanetary Currents Sheets at 1 AU', *J. Geophys. Res.* **82**, 3191.

Cargill, P. J. and Eastman, T. E.: 1991, 'The Structure of Tangential Discontinuities. 1. Results of Hybrid Simulations', *J. Geophys. Res.* **96**, 13763.

Channell, P. J.: 1976, 'Exact Vlasov–Maxwell Equilibria with Sheared Magnetic Field', *Phys. Fluids* **19**, 1541.

Coppi, B., Mark, J. W.-K., Sugiyama, L., and Bertin, G.: 1979, 'Reconnecting Modes in Collisionless Plasmas', *Phys. Rev. Letters* **42**, 1058.

Davidson, R. C., Gladd, N. T., Wu, C. S., and Huba, J. D.: 1977, 'Effects of Finite Plasma Beta on the Lower Hybrid Drift Instability', *Phys. Fluids* **20**, 301.

De Keyser, J., Roth, M., Lemaire, J. L., Tsurutani, B. T., Ho, C. M., and Hammond, C. M.: 1995, 'Theoretical Plasma Distributions Consistent with Ulysses Magnetic Field Observations in a Solar Wind Tangential Discontinuity', *Aeronomica Acta*, Belgian Institute for Space Aeronomy, Brussels.

Drake, J. F. and Lee, Y. C.: 1977, 'Kinetic Theory of Tearing Instabilities', *Phys. Fluids* **20**, 1341.

Drake, J. F., Gerber, J., and Kleva, R. G.: 1994, 'Turbulence and Transport in the Magnetopause Current Layer', *J. Geophys. Res.* **99**, 211.

Dubinin, E. M., Podgorny, I. M., and Potanin, Y. N.: 1980, 'Structure of the Magnetic Field at the Boundary of the Magnetosphere: Analysis of a Simulation Experiment', *Cosmic Res., Engl. Transl.* **18**, 99.

Eastman, T. E., Frank, L. A., Peterson, W. K., and Lennartsson, W.: 1984, 'The Plasma Sheet Boundary Layer', *J. Geophys. Res.* **89**, 1553.

Elphinstone, R. D., Hearn, D., Murphree, J. S., and Cogger, L. L.: 1991, 'Mapping Using the Tsyganenko Long Magnetospheric Model and Its Relationship to Viking Auroral Images', *J. Geophys. Res.* **96**, 1467.

Fälthammar, C.-G., Akasofu, S.-I., and Alfvén, H.: 1978, 'The Significance of Magnetospheric Research for Progress in Astrophysics', *Nature* **275**, 185.

Furth, H. P., Killeen, J., and Rosenbluth, M. N.: 1963, 'Finite-Resistivity Instabilities in a Sheet Pinch', *Phys. Fluids* **6**, 459.

Galeev, A. A. and Zelenyi, L. M.: 1977, 'The Model of Magnetic Field Reconnection in a Slab Collisionless Plasma Sheath', *Pis'ma Zh. Eksperim. Teor. Fiz.* **25**, 407.

Galeev, A. A., Kuznetsova, M. M., and Zelenyi, L. M.: 1986, 'Magnetopause Stability Threshold for Patchy Reconnection', *Space Sci. Rev.* **44**, 1.

Gary, S. P. and Eastman, T. E.: 1979, 'The Lower Hybrid Drift Instability at the Magnetopause', *J. Geophys. Res.* **84**, 7378.

Gladd, N. T.: 1990, 'Collisionless Drift-Tearing Modes in the Magnetopause', *J. Geophys. Res.* **95**, 889.

Gosling, J. T., Thomsen, M. F., Bame, S. J., Elphic, R. C., and Russell, C. T.: 1990, 'Plasma Flow Reversals at the Dayside Magnetopause and the Origin of Asymmetric Polar Cap Convection', *J. Geophys. Res.* **95**, 8073.

Grad, H.: 1961, 'Boundary Layer between a Plasma and a Magnetic Field', *Phys. Fluids* **4**, 1366.

Greenly, J. B. and Sonnerup, B. U. Ö.: 1981, 'Tearing at the Magnetopause', *J. Geophys. Res.* **86**, 1305.

Gurnett, D. A., Anderson, R. R., Tsurutani, B. T., Smith, E. J., Paschmann, G., Haerendel, G., Bame, S. J., and Russell, C. T.: 1979, 'Plasma Wave Turbulence at the Magnetopause: Observations from ISEE 1 and 2', *J. Geophys. Res.* **84**, 7043.

Harris, E. G.: 1962, 'On a Plasma Sheath Separating Regions of Oppositely Directed Magnetic Field', *Nuovo Cimento* **23**, 115.

Huba, J. D., Gladd, N. T., and Papadopoulos, K.: 1978, 'Lower Hybrid Drift Turbulence in the Distant Magnetotail', *J. Geophys. Res.* **83**, 5217.

Hudson, P. D.: 1970, 'Discontinuities in an Anisotropic Plasma and Their Identification in the Solar Wind', *Planetary Space Sci.* **18**, 1611.

Kan, J. R.: 1972, 'Equilibrium Configurations of Vlasov Plasmas Carrying a Current Component Along an External Magnetic Field', *J. Plasma Phys.* **7**, 445.

Kuznetsova, M. M. and Roth, M.: 1995, 'Thresholds for Magnetic Percolation through the Magnetopause Current Layer in Asymmetrical Magnetic Fields', *J. Geophys. Res.* **100**, 155.

Kuznetsova, M. M. and Zelenyi, L. M.: 1985, 'Stability and Structure of the Perturbations of the Magnetic Surfaces in the Magnetic Transitional Layers', *Plasma Phys. Controlled Fusion* **27**, 363.

Kuznetsova, M. M. and Zelenyi, L. M.: 1990a, 'The Theory of FTE: Stochastic Percolation Model' in C. T. Russell, E. R. Priest, and L. C. Lee, ed(s)., *Physics of Magnetic Flux Ropes, Geophys. Monogr. Ser., Vol. 58*, AGU, Washington, D.C., p. 473.

Kuznetsova, M. M. and Zelenyi, L. M.: 1990b, 'Nonlinear Evolution of Magnetic Islands in a Sheared Magnetic Field with Uniform Plasma Background', *Plasma Phys. Controlled Fusion* **32**, 1183.

Kuznetsova, M. M., Roth, M., and Zelenyi, L. M.: 1995, 'Kinetic Structure of the Magnetopause: Equilibrium and Percolation' in P. Song, B. U. Ö. Sonnerup, and M. F. Thomsen, ed(s)., *Physics of the Magnetopause, Geophys. Monogr. Ser., Vol. 90*, AGU, Washington, D.C., p. 99.

Kuznetsova, M. M., Roth, M., Wang, Z., and Ashour-Abdalla, M.: 1994, 'Effect of the Relative Flow Velocity on the Structure and Stability of the Magnetopause Current Layer', *J. Geophys. Res.* **99**, 4095.

Lakhina, G. S., and Schindler, K.: 1983a, 'Collisionless Tearing Modes in the Presence of Shear Flow', *Astrophys. Space Sci.* **89**, 293.

Lakhina, G. S. and Schindler, K.: 1983b, 'Tearing Modes in the Magnetopause Current Sheet', *Astrophys. Space Sci.* **97**, 421.

Laval, G., Pellat, R., and Vuillemin, M.: 1966, 'Instabilités électromagnétiques des plasmas sans collisions', *Plasma Phys. and Contr. Fusion Res., IAEA, Vienna* **2**, p. 259.

Lee, L. C. and Kan, J. R.: 1979, 'A Unified Kinetic Model of the Tangential Magnetopause Structure', *J. Geophys. Res.* **84**, 6417.

Lemaire, J. and Burlaga, L. F.: 1976, 'Diamagnetic Boundary Layers: a Kinetic Theory', *Astrophys. Space Sci.* **45**, 303.

Lemaire, J., Roth, M., Scherer, M., and Schulz, M.: 1983, 'Interdisciplinary Study of Directional Discontinuities in the Solar Wind with ISPM' in K.-P. Wenzel, R.G. Marsden, and B. Battrick, ed(s)., *The International Solar Polar Mission —Its Scientific Investigations*, European Space Agency, ESA SP-1050, p. 263.

Lembege, B. and Pellat, R.: 1982, 'Stability of a Thick Two-Dimensional Quasi-Neutral Sheet', *Phys. Fluids* **25**, 1995.

Lyons, L. R.: 1981, 'Discrete Aurora as the Direct Result of an Inferred, High-Altitude Generating Potential Distribution', *J. Geophys. Res.* **86**, 1.

Lyons, L. R., Evans, D. S., and Lundin, R.: 1979, 'An Observed Relation Between Magnetic Field Aligned Electric Fields and Downward Electron Energy Fluxes in the Vicinity of Auroral Forms', *J. Geophys. Res.* **84**, 457.

McBride, J. B., Ott, E., Boris, J. P., and Orens, J. H.: 1972, 'Theory and Simulation of Turbulent Heating by the Modified Two-Stream Instability', *Phys. Fluids* **15**, 2367.

Morse, R. L.: 1965, 'Adiabatic Time Development of Plasma Sheaths', *Phys. Fluids* **8**, 308.

Nicholson, R. B.: 1963, 'Solution of the Vlasov Equations for a Plasma in a Uniform Magnetic Field', *Phys. Fluids* **6**, 1581.

Parks, G. K., Fitzenreiter, R., Ogilvie, K. W., Huang, C., Anderson, K. A., Dandouras, J., Frank, L. A., Lin, R. P., McCarthy, M., Rème, H., Sauvaud, J. A., and Werden, S.: 1992, 'Low-Energy Particle Layer Outside of the Plasma Sheet Boundary', *J. Geophys. Res.* **97**, 2943.

Paschmann, G., Sckopke, N., Haerendel, G., Papamastorakis, J., Bame, S. J., Asbridge, J. R., Gosling, J. T., Hones, E. W., Jr., and Tech, E. R.: 1978, 'ISEE Plasma Observations Near the Subsolar Magnetopause', *Space Sci. Rev.* **22**, 717.

Press, W. H., Flannery, B. P., Teukolsky, S. A., and Vetterling, W. T.: 1986, *Numerical Recipes. The Art of Scientific Computing*, Cambridge University Press, Cambridge.

Quest, K. B. and Coroniti, F. V.: 1981a, 'Tearing at the Dayside Magnetopause', *J. Geophys. Res.* **86**, 3289.

Quest, K. B. and Coroniti, F. V.: 1981b, 'Linear Theory of Tearing in a High-Beta Plasma', *J. Geophys. Res.* **86**, 3299.

Ralston, A. et Wilf, H. S.: 1965, *Méthodes mathématiques pour calculateurs arithmétiques*, Dunod, Paris, p. 482.

Rosenbluth, M. N., Sagdeev, R. Z., Taylor, J. B., and Zaslavsky, G. M.: 1966, 'The Destruction of Magnetic Surfaces', *Nucl. Fusion* **6**, 297.

Roth, M.: 1976, 'The Plasmapause as a Plasmasheath: a Minimum Thickness', *J. Atmospheric Terrest. Phys.* **38**, 1065.

Roth, M.: 1978, 'Structure of Tangential Discontinuities at the Magnetopause: the Nose of the Magnetopause', *J. Atmospheric Terrest. Phys.* **40**, 323.

Roth, M.: 1979, 'A Microscopic Description of Interpenetrated Plasma Regions' in B. Battrick and J. Mort, ed(s)., *Magnetospheric Boundary Layers*, European Space Agency, ESA SP–148, pp. 295–309.

Roth, M.: 1984, 'La structure interne de la magnétopause', *Mém. Cl. Sci. Acad. R. Belg. Collect. 8°* **44(7)**, 222. Also in: *Aéronomica Acta A, 221*, Belgian Institute for Space Aeronomy, 1980.

Roth, M.: 1983, 'Boundary Layers in Space Plasmas: a Kinetic Model of Tangential Discontinuities' in W. Botticher, H. Wenk, and E. Schulz-Gulde, ed(s)., *Phenomena in Ionized Gases, XVI International Conference*, Dusseldorf, pp. 139–147.

Roth, M.: 1986, 'A Computer Simulation Study of the Microscopic Structure of a Typical Current Sheet in the Solar Wind' in R. G. Marsden, ed(s)., *The Sun and the Heliosphere in Three Dimensions, ASSL123*, D. Reidel Publ. Co., Dordrecht, Holland, pp. 167–171.

Roth, M., Evans, D. S., and Lemaire, J.: 1993, 'Theoretical Structure of a Magnetospheric Plasma Boundary: Application to the Formation of Discrete Auroral Arcs', *J. Geophys. Res.* **98**, 411.

Roth, M., Lemaire, J., and Misson, A.: 1990, 'An Iterative Method to Solve the Nonlinear Poisson's Equation in the Case of Plasma Tangential Discontinuities', *J. Comput. Phys.* **86**, 466.

Russell, C. T. and Elphic, R. C.: 1978, 'Initial ISEE Magnetometer Results: Magnetopause Observations', *Space Sci. Rev.* **22**, 681.

Sestero, A.: 1964, 'Structure of Plasma Sheaths', *Phys. Fluids* **7**, 44.

Sestero, A.: 1966, 'Vlasov Equation Study of Plasma Motion Across Magnetic Fields', *Phys. Fluids* **9**, 2006.

Sonnerup, B. U. Ö. and Cahill, L. J., Jr.: 1968, 'Explorer 12 Observations of the Magnetopause Current Layer', *J. Geophys. Res.* **73**, 1757.

Southwood, D. J., Saunders, M. A., Dunlop, M. W., Mier-Jedrzejowicz, W. A. C., and Rijnbeek, R. P.: 1986, 'A Survey of Flux Transfer Events Recorded by the UKS Spacecraft Magnetometer', *Planetary Space Sci.* **34**, 1349.

Su, S. Y. and Sonnerup, B. U. Ö.: 1968, 'First-Order Orbit Theory of the Rotational Discontinuity', *Phys. Fluids* **11**, 851.

Szabo, A., Lepping, R. P., Peredo, M., and Byrnes, J.: 1995, 'Improvements and Extensions of the Heliospheric Current Sheet Study with the WIND Magnetometer Measurements' in , ed(s)., *EOS Supplement, Transactions, American Geophysical Union, Vol. 76*, AGU, p. 218. Abstract of paper SH21B-2 presented at the Spring Meeting of the American Geophysical Union, Baltimore, 1995.

Treumann, R. A., LaBelle, J., and Bauer, T. M.: 1995, 'Diffusion Processes: an Observational Perspective' in P. Song, B. U. Ö. Sonnerup, and M. F. Thomsen, ed(s)., *Physics of the Magnetopause, Geophys. Monogr. Ser., Vol. 90*, AGU, Washington, D.C., p. 331.

Tsurutani, B. T., Ho, C. M., Smith, E. J., Neugebauer, M., Goldstein, B. E., Mok, J. S., Arballo, J. K., Balogh, A., Southwood, D. J., and Feldman, W. C.: 1994, 'The Relationship between Interplanetary Discontinuities and Alfvén Waves: Ulysses Observations', *Geophys. Res. Letters* **21**, 2267.

Wang, Z. and Ashour-Abdalla, M.: 1992, 'Topological Variation in the Magnetic Field Line at the Dayside Magnetopause', *J. Geophys. Res.* **97**, 8245.

Wang, Z. and Ashour-Abdalla, M.: 1994, 'Magnetic Field Line Stochasticity at the Magnetopause', *J. Geophys. Res.* **99**, 2321.

Whipple, E. C., Hill, J. R., and Nichols, J. D.: 1984, 'Magnetopause Structure and the Question of Particle Accessibility', *J. Geophys. Res.* **89**, 1508.

Winske, D., Thomas, V. A., and Omidi, N.: 1995, 'Diffusion at the Magnetopause: a Theoretical Perspective' in P. Song, B. U. Ö. Sonnerup, and M. F. Thomsen, ed(s)., *Physics of the Magnetopause, Geophys. Monogr. Ser., Vol. 90*, AGU, Washington, D.C., p. 321.

Wu, C. S., Zhou, Y. M., Tsai, S. T., Guo, S. C., Winske, D., and Papadopoulos, K.: 1983, 'A Kinetic Cross-Field Streaming Instability', *Phys. Fluids* **26**, 1259.

Zelenyi, L. M. and Kuznetsova, M. M.: 1984, 'Large-scale Instabilities of the Plasma Sheet Driven by Particle Fluxes at the Boundary of the Magnetosphere', *Fiz. Plasmy Moscow* **10**, 190.

Zelenyi, L., Kovrazkhin, R., and Bosqued, J.: 1990, 'Velocity-Dispersed Ion Beams in the Nightside Auroral Zone: AUREOL 3 Observations', *J. Geophys. Res.* **95**, 119.